Comparison of Different Coupling Methods for Joint Inversion of Geophysical data: A case study for the Namibian Continental Margin

G. Franz[1], M. Moorkamp[2], M. Jegen[1], C. Berndt[1], W. Rabbel[3]

[1]GEOMAR Helmholtz Centre for Ocean Research Kiel

[2]Ludwig-Maximilians University of Munich, Germany

[3]Christian-Albrechts University Kiel, Germany

Corresponding author: Gesa Franz (gfranz@geomar.de)

Key Points:

- imaging of rift related volcanic processes at the Namibian margin through joint analysis of magnetotelluric, gravity and seismic data
- 3D inversion of marine magnetotelluric data is improved by cross-gradient coupling with fixed structural density model

Abstract

Integration of multiple geophysical methods in combined data analysis is a key practice to reduce model uncertainties and enhance geological interpretations. Electrical resistivity models resulting from inversion of marine magnetotelluric (MT) data, often lack depth resolution of lithological boundaries, and distinct information for shallow model parts. This is due to the nature of the physics i.e. diffusive method, model regularization during inversion, and survey setup i.e. large station spacing and missing high frequency data. Thus, integrating data or models to constrain layer thicknesses or structural boundaries is an effective approach to derive better constrained, more detailed resistivity models. We investigate the different impacts of three cross-gradient coupled constraints on 3D MT inversion of data from the Namibian passive continental margin. The three constraints are a) coupling with a fixed structural density model; b) coupling with satellite gravity data; c) coupling with a fixed gradient velocity model. Here we show that coupling with a fixed model (a and c) improves the resistivity model most. Shallow conductors imaging sediment cover are confined to a thinner layer in the resulting resistivity models compared to the MT-only model. Additionally these constraints help to suppress vertical smearing of a conductive anomaly attributed to a fracture zone, and clearly show that the seismically imaged Moho is not accompanied by a change in electrical resistivity. All of these observations aid interpretation of an Earth model indicating involvement of a plume impact in continental break-up during the early Cretaceous.

1 Introduction

Different geophysical data describe different physical properties of the Earth that are not necessarily dependent on each other. Electromagnetic data depend on the electrical resistivity of the subsurface, gravity data on density variations, and seismic data on seismic velocity and density variations. Normally, there are many physical parameter models that fit the observed data, because there are fewer measurements than necessary to derive a unique model, i.e. the problem is under-constrained and the measured data are associated with errors. Also, the governing physics may limit the various geophysical methods, e.g. diffusive methods such as electromagnetic measurements cannot resolve sharp boundaries, gravity data have a limited depth resolution, and seismic data provide limited velocity information for short observation

distances. As a result, simplified (1D, 2D and/or smoothed) earth models are used both as a starting and end point in the geophysical data evaluation. For these reasons, interpreters are always confronted with ambiguity when analyzing physical parameter models arising from different geophysical data.

There are two approaches for deriving Earth models from observed data: iterative forward modeling and inversions. The first describes techniques, where the theoretical data responses are calculated for a constructed physical parameter model with a given measurement geometry (e.g. Götze & Lahmeyer, 1988; Zelt, 1999). The parameter model construction heavily depends on the experience and expertise of the interpreter. The difference between the observed data and the calculated forward modeling result is usually quantified as the so-called data misfit. The misfit is a measure how well the physical model represents the observed data. An inversion describes a procedure in which a physical parameter model is calculated automatically in form of an optimization problem (Tarantola, 2005). This requires the formulation of a so-called objective function which mathematically describes the desired properties of the resulting model. Typical objective functions consist of three terms. First, there is a data misfit term that describes how well the final model is consistent with the observed data. Then there is a regularization term which keeps the model simple, for example by reducing spatial parameter variations and suppressing the influence of noisy data. Finally, if multiple physical parameters are involved, a coupling term describes the relationship between those parameters (e.g. Moorkamp, 2017). Either stochastic or deterministic methods are used to identify the minima of objective function. Stochastic methods sample the entire possible solution space and yield a probability distribution for all model parameters that fit the data. These methods have the advantage that a global minimum can be distinguished from a local minimum and offers the possibility to a) identify error bars on the physical parameter model values fitting the data, hence evaluate the resolution of model features and b) identify correlations between model parameters. However, for large problems with many model parameters, stochastic approaches requiring many forward calculations are computationally highly expensive (Mosegaard & Tarantola, 1995; Ulrych et al., 2001). Also, for complex models the results are difficult to visualize or analyze. Deterministic inversion methods solve iteratively the inverse problem from a given starting model. First, the value of the objective function and its associated gradient with respect to the model parameters are calculated. This gradient is then used to improve the previous model by finding an

adjustment that reduces the value of the objective function. The procedure is repeated until a final minimum misfit is reached (Nocedal & Wright, 2006; Tarantola, 2005). The advantage of a deterministic procedure is that it requires a small number of forward calculations and that it is therefore - compared to stochastic methods - numerically cheap. However, there are a number of disadvantages associated with this methodology: a) the local search procedure does not provide information whether the resulting minimum misfit model is associated with a local or global minimum; b) the resulting best fitting model often depends on the starting model, particularly for low resolution geophysical methods or large number of model parameters; and c) there is limited information on the resolution of the model parameters.

Additional constraints to the inversion of geophysical data may help to increase the plausibility of the resulting models, limit the solution space, and decrease the ambiguity of models. In this paper we refer to all different ways to conduct this integration as “joint inversion”, where the resulting Earth model is required to explain several data sets or models at once. The constraints can either be applied by integrating an additional geophysical data set in the inversion procedure (Günther & Rücker, 2006; Heincke et al., 2017; Moorkamp, 2017; Shi et al., 2017) or by integrating a physical Earth model that was derived independently from another geophysical data set (Bedrosian, 2007; Kalscheuer et al., 2015; Mandolesi & Jones, 2014; Zhou et al., 2015), which is sometimes called cooperative inversion. Joint inversion can either be applied to different geophysical data sets depending on the same physical parameters, i.e. electrical resistivity (Candansayar & Tezkan, 2008) or seismic velocities (Parolai et al., 2005), or on a combination of data sets that measure different physical parameters (Günther & Rücker, 2006; Heincke et al., 2017; Moorkamp, 2017; Shi et al., 2017). A link in joint inversion for the latter can either be enforced by assuming a parameter relationship between physical parameters or by requiring a similar structure, i.e. enforcing changes in the physical parameters at the same spatial position in the different physical parameter models (e.g., Gallardo & Meju, 2003; Moorkamp, 2017).

In this paper, we apply different joint inversion schemes to data sets acquired along the Namibian continental margin (Figure 1). The passive margin setting is well suited for joint data analysis because of a high variability in lithology and physical properties. Complex geological processes during the opening of the South Atlantic such as extension, crustal breakup and mantle upwelling formed distinct geological structures, e.g. fault zones or thinned crust, while partial

112 melting, magma accumulation and volcanism led to various magmatic and volcanic structures.
113 Post-break-up cooling and subsidence have affected the margin, for example by controlling the
114 location of sedimentary depocenters. Parameters such as mineral composition, porosity, fluid
115 content, and ambient temperature of the geological features affect the measurable physical
116 properties such as seismic velocity, resistivity, or density. Therefore, the geological processes
117 that led to variations in these parameters can be investigated using different geophysical data
118 sets.

119 A wide range of different geophysical surveys have been carried out along the Namibian
120 Margin. They image the crustal- and upper mantle structure both on- and offshore to investigate
121 the break-up related features. Seismic studies revealed magmatic geological features such as the
122 hot spot trail Walvis Ridge, seaward dipping reflectors caused during the initial subaerial stage
123 of break-up volcanism (Gladczenko et al., 1998; Elliot et al., 2009), lower crustal high velocity
124 bodies interpreted as magmatic underplating (Bauer et al., 2000; Gladczenko et al., 1998; Planert
125 et al., 2016) ,high v_P/v_S ratio, (Heit et al., 2015), and thickened oceanic crust caused by the late
126 stage of break-up volcanism (Fromm et al., 2017). The gravity modeling study by Maystrenko et
127 al. (2013) imaged high density lower crustal intrusions. Inversion of magnetotelluric (MT) data
128 by Kapinos et al. (2016) and Jegen et al. (2016) shows high resistivities in the middle and deep
129 crust indicative of magmatic processes. While all of these models show similarity concerning the
130 lateral extent of imaged magmatic features, little coherence exists concerning the vertical extent
131 and depth of the geological targets (Jegen et al., 2016).

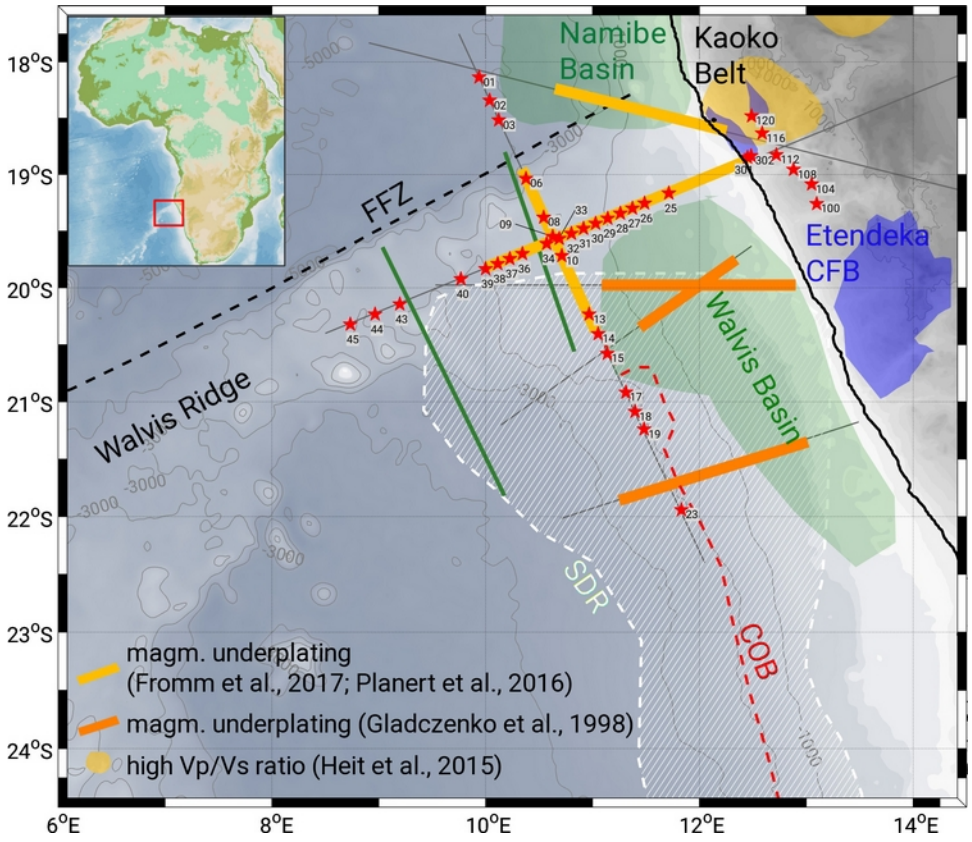

Figure 1. Overview map of geological and geophysical features along the Namibian coast. Large scale tectonic features are the Walvis Ridge and Kaoko Belt. Blue areas show the extent of the continental flood basalts. Green areas are sedimentary basins. FFZ (Florianopolis Fracture Zone) and COB (continent-ocean boundary) are taken from Fromm et al. (2015) and Gladczenko et al. (1998), respectively and the SDR extent is a combination of Elliott et al. (2009), Bauer & Schulze (1996) and Gladczenko et al. (1998). Orange color marks evidences for magmatic underplating. The circular shapes onshore mark the high vp/vs structures by Heit et al. (2015), light orange profile lines are the thickened crust and high velocity lower crustal bodies identified by Fromm et al. (2015) and Planert et al. (2016); and the dark orange profiles are the high velocity lower crustal bodies determined by Gladczenko et al. (1998). Green lines are two seismic profiles interpreted by Goslin et al. (1974). Red stars with numbers show the positions of MT stations: perpendicular to the coast is profile P100, parallel to the coast is profile P3.

Of all these available data, the MT measurements are the only dataset with both 3D coverage and depth resolution. They also have the largest depth penetration. However, magnetotelluric responses are governed by a diffusive equation, and the method's spatial resolution is limited. Thus, there is a large range of resistivity models which fit the MT data. Since 3D deterministic inversion of the MT data only yields one 3D resistivity model, a verification that this possible solution is closest to the true Earth model requires input of additional information. Options for this verification are limited by the fact that other geophysical data and parameter models that may be used for joint inversion also have disadvantages. For example the aforementioned seismic data are only available in 2D and only image down to the Moho. Furthermore, the results are based on several different data analysis methods, e.g. Fromm et al. (2017) used forward velocity- and gravity modeling while Planert et al. (2016) performed 2D tomographic inversion. The gravity data yield 3D models, but have very little depth sensitivity. Therefore, comparison of the resulting physical models is difficult. They have different spatial resolution and sensitivities, and they cover different scales. A combination of all these data should nevertheless improve interpretation and resolve an Earth model closest to the "true model", because the advantages of the different methods may partly compensate the disadvantages and ambiguities of other methods. In this paper we present a study combining the MT inversion with other acquired geophysical data in joint inversion approaches in order to limit the model solution space and test the feasibility of features observed in the inverted models based on MT data only.

We implement four separate deterministic inversion approaches to evaluate the benefits of different constraints in 3D MT inversions. The reference is a single method inversion of the MT data (MT-only), and the three joint inversion approaches are: JI1: constraining MT inversion with the 3D structural density reference model derived from gravity modeling by Maystrenko et al. (2013), JI2: jointly inverting the marine MT- with satellite gravity data, and JI3: combining the gradient 2D velocity reference model by Fromm et al. (2017) with the 3D MT inversion. To account for the dimensional difference (2D versus 3D) in the latter, the MT inversion is conducted on a narrow "quasi-2D" cube around one profile's stations and seismic velocities are extended to both sides of the profile to form a pseudo 3D model.

Coupling of the different methods is realized using the cross-gradient method by Gallardo & Meju (2003), which offers a technique for structural coupling of two models, but represents a

rather weak form of coupling. Due to the complex geology in the continental margin regime, defining distinct and commonly valid parameter relationships to convert from velocity to density and resistivity or vice versa is extremely difficult. Therefore, stronger coupling mechanisms based on a physical parameter relationship could not be used. However, if geological regimes and relationships between their physical parameters can be derived by the presented structural joint inversion, parameter-relationship constrained joint inversion might be possible in the future, and enable fine-tuning of inversion results.

Our study aims to achieve two main goals: a) we want to improve the Namibian Margin Earth model regarding the geological features related to continental break-up, and b) we aim to investigate the impacts of different joint inversion coupling constraints on the resulting inversion models. Based on these goals, this paper focuses on three main objectives:

1. How can we improve the 3D resistivity model from single method MT inversion to gain new insights and which inversion constraints can benefit geological interpretations?

2. How do cross-gradient coupling of MT data inversion with the fixed structural density model (JI1), and cross-gradient coupled joint inversion of MT and gravity data differ (JI2)?

3. What is the impact of two different types of fixed models (structural density-, and gradient velocity model, i.e. JI1 and JI3) as cross-gradient coupled model constraints on MT data inversion?

We first discuss the data sets considered in the analysis as well as the pre-existing models which we apply as model constraints in our joint inversion. Subsequently, we describe the joint inversion algorithm applied to the data. The results section is structured in three sections focused on i) weighting parameters and misfit evolution, ii) data fit of the resulting inversion models, and iii) comparison of the models. For our discussion, we evaluate the model differences by comparing with reference models and other geophysical interpretations, also discussing data fits and sensitivity.

2 Data and Reference Models

In the following section, we introduce the MT and gravity data sets that we invert separately and in a joint approach, and the processing applied to them prior to inversion. We also describe two parameter models, i.e. the 3D structural density model and a 2D local velocity

model, which are used as independent and external model structural constraints in a constrained inversion of our MT data.

2.1 MT input data

The resistivity models presented here, are based on data from 32 marine MT stations collected during two cruises on RV Maria S. Merian (MSM 17-1 and MSM 17-2) from November 2010 to January 2011 (see Jegen et al., 2016). The stations were deployed along two orthogonal seismic profiles to image the structure along (profile 100) and across (profile 3) Walvis Ridge (Fig. 1). Also, we have included data from eight land-based MT stations, deployed by GFZ Potsdam in October and November 2011 (see Kapinos et al., 2016) to expand the investigated area onshore and account for the electromagnetic coast effect, which arises due to the big resistivity contrast of seawater adjacent to continental crust (Ferguson et al., 1990; Worzewski et al., 2012).

Data processing consists of data rotation, impedance calculation and dimensionality analysis. The marine MT data were corrected for the instrument's tilt and rotated to a common coordinate system pointing north (Jegen et al., 2016). Impedance calculation and dimensionality analysis were carried out with the algorithms described by Chave & Thomson (2004); Egbert (1997), and Martí et al. (2009). The onshore stations' processing was conducted by Kapinos et al. (2016) with procedures described in Becken & Burkhardt (2004); Ritter et al. (1998); Weckmann et al. (2005). Due to limited survey time, the stations of profile 100 include data only up to 10000 s and the eight land stations up to 1000 s. However, the MT stations along profile 3 cover periods up to 50000 s. We interpolated all data for 16 periods ranging from ~30 to 5·104 s and replace missing data, particularly large period data for land- and profile 100 stations, by dummy values with large errors. Dimensionality analysis indicates a clear three-dimensional character of the marine data (Jegen et al., 2016). Hence, all subsequent work had to concentrate on 3D processing, despite the original survey planning along two 2D profiles.

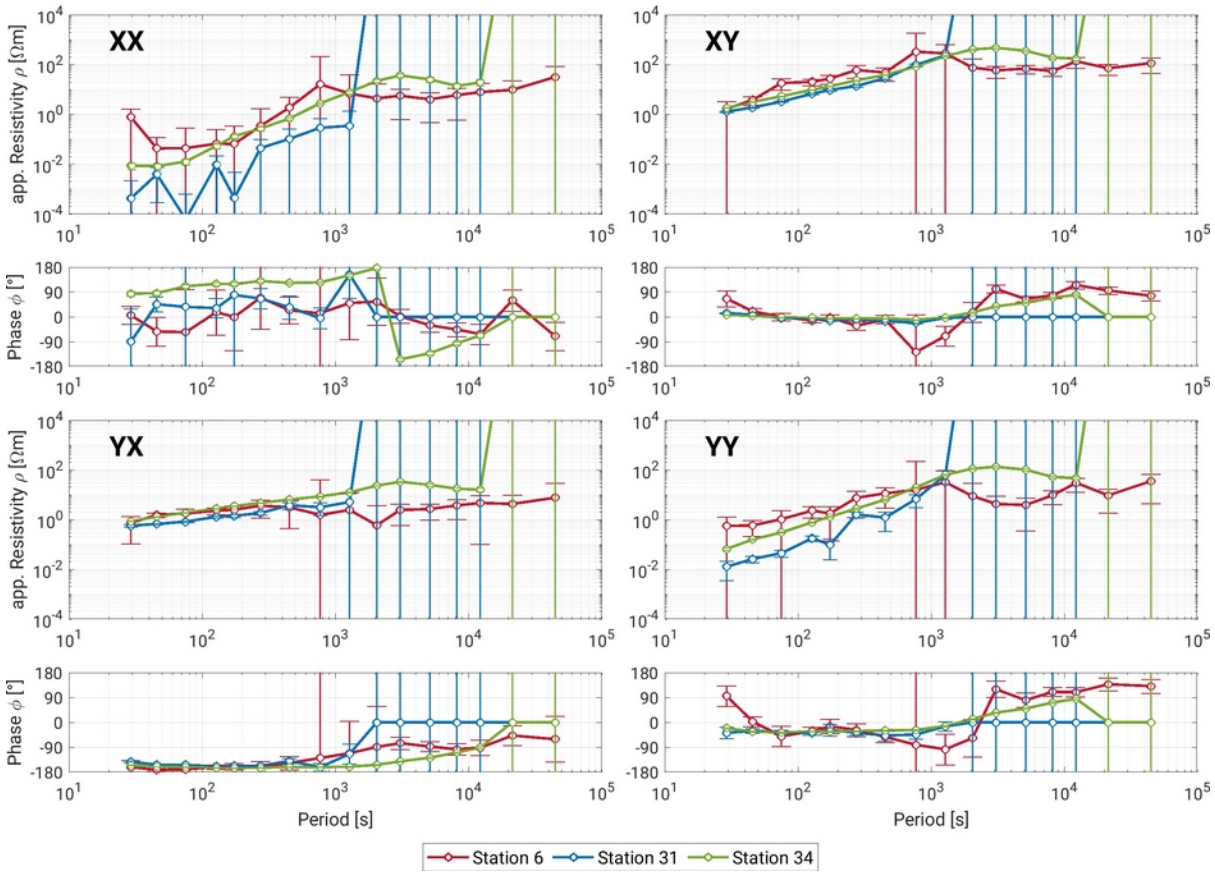

Figure 2. Apparent resistivity and phase for three marine MT stations with varying quality: Station 34 (green) as an example for high data quality, stations 31 (blue) as an example for medium quality with lacking high periods, and station 6 (red) as an example for poor data quality.

MT data quality variations are displayed in Figure 2 for three marine stations. Station 34 (green) is an example of a good quality data set, exhibiting smooth apparent resistivity and phase curves and small errors. Station 31 data (blue) has larger errors and more rugged curves in the XX component but shows good data quality in the other components up to periods of ~1000 s. Impedance values at longer periods could not be derived at this station. Finally, station 6 (red) represents stations with poor data quality. All four components, resistivity and phase curves are not smooth and we observe high errors in all components and various frequencies.

2.2 Gravity input data

We use satellite gravity data as input for the gravity inversion. The data set used is based on the high-resolution EIGEN-6C4 global field model, which is derived from a combination of

the satellite gravity missions LAGEOS (Cohen & Smith, 1985), GRACE (Tapley et al., 2004) and GOCE (Drinkwater et al., 2007) as well as DTU ground data (Andersen et al., 2010; Förste et al., 2014). We use a spherical approximation of the anomaly at 3000 m height above sea level on a 0.1 x 0.1 degree grid (Barthelmes & Köhler, 2016; Ince et al., 2019) as depicted in Figure 3, upper left panel. This height is suitable, because we want to remove the effect of the onshore topography, and therefore need to be well above the highest elevation. The effect of topography on the gravity data is clearly visible in Figure 3 (top left), as gravity highs (red colors) follow the bathymetry lines around Walvis Ridge, several seamounts, as well as the onshore topography around Brandberg Mountain (~21.1°S, 14.5°E) and the mountain ranges of the Kaokoveld desert at the Angolan border. The data are also influenced significantly by different average densities of continental – (2810 kg/m^3), and oceanic crust (2900 kg/m^3) as well as deeper Moho depths for continents (~40 km) compared to the oceanic regime (~10 km).

In order to resolve underlying density variations of interest, the satellite data need to be corrected for the effect of topography/bathymetry (equivalent to Bouguer correction), as well as for the effect of variation in Moho depth. For both corrections we calculated the vertical gravitational component g_z of a correction model at 3000 m using the forward modeling code Tesseroids (Uieda et al., 2016) and subtract the responses from the input satellite gravity data. The correction model is illustrated in Figure 4 (top right). Topographic heights and water depth for the first correction were extracted from a spherical harmonic expansion of the ETOPO1 model on a 0.1 x 0.1 degree grid. Topographic heights (above 0 m) were assigned a value of 2810 kg/m^3 (reference crustal density) and oceanic regions were corrected with a value of -1780 kg/m^3, i.e. the difference between an assumed water density of 1030 kg/m^3 and reference crustal density of 2810 kg/m^3. The resulting topography effect response is shown in the top right of Figure 3. After subtracting this effect from the input data, the residual gravity anomaly is dominated by the difference of the continental and oceanic crust.

To account for this continent-ocean difference, we corrected for the crustal thickness effect on gravity, i.e. crustal thickness varies from ~10 km in the oceanic domain to ~40 km onshore, by creating a second correction model. Areas with a Moho shallower than reference (35 km) were compensated with a density of 412 kg/m^3 (the difference between reference crustal- and mantle density (2810 kg/m^3 and 3222 kg/m^3) and areas with a deeper Moho with a density of - 412 kg/m^3. By using these two constant values we presume that due to the old age of the crust,

lithospheric cooling has reached equilibrium in the survey area and no thermally induced lateral density variations exist anymore. The 3D Moho depths used in the correction were derived from a combination of a smoothed version of the structural density model presented in Maystrenko et al. (2013) and the global CRUST1 model (Laske et al., 2013). This combination allows us to take differences of continental- and oceanic crustal thickness as well as the thickened crust below the eastern part of Walvis Ridge into account. The gravity effect of the Moho depth compensation is shown on the lower left panel in Figure 3. The final vertical gravity anomaly derived after subtracting the topographic and crustal correction responses are shown in the lower right panel of Figure 3. The corrected gravity anomaly data were used as the input gravity data for the subsequent joint inversions wherever gravity data are considered. The two most obvious features of the corrected gravity map are the strong positive gravity anomaly at the landfall of Walvis Ridge, and a clear negative gravity anomaly in the southern Walvis Basin.

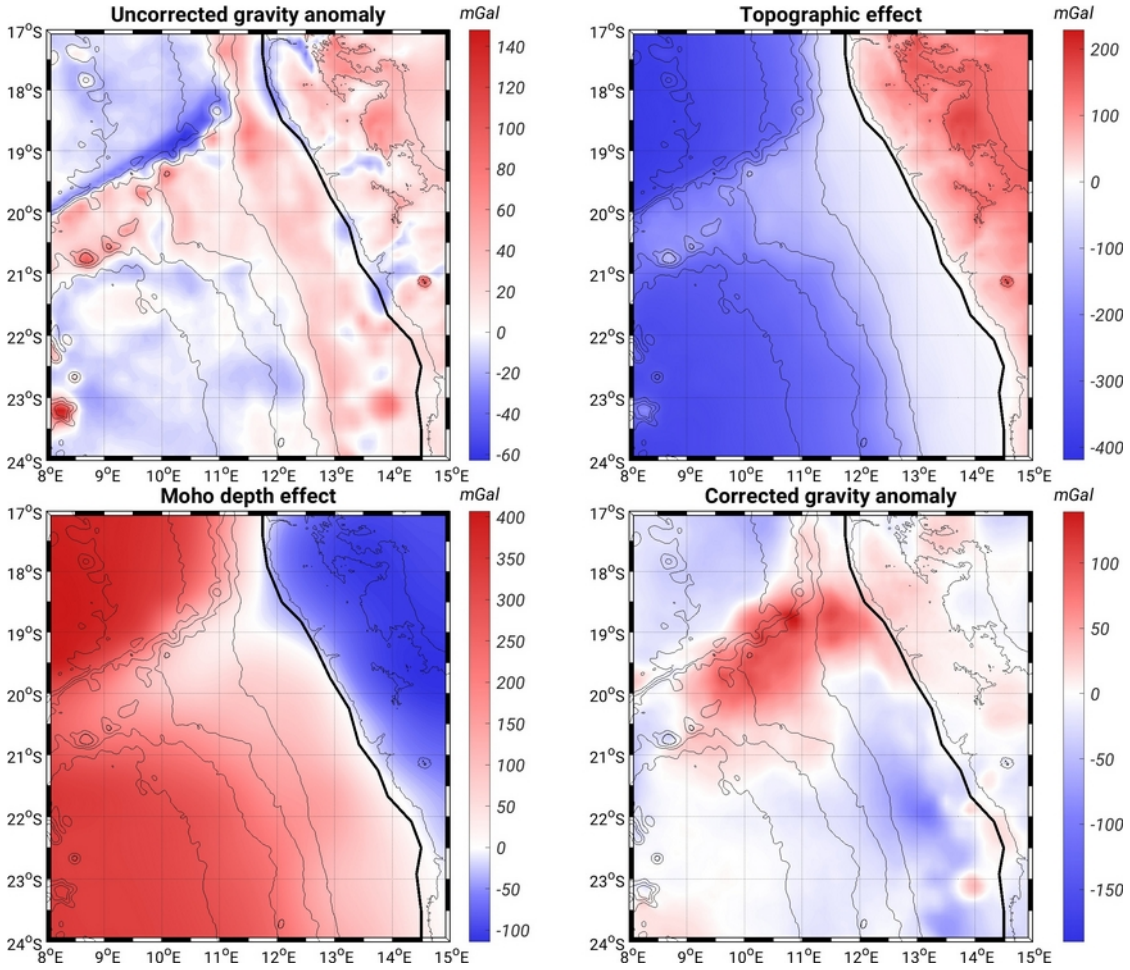

Figure 3. Gravity data and corrections. Upper left panel is spherical approximation of gravity anomaly. Upper right is the calculated effect of topography and bathymetry. Lower left is the effect of Moho depth. Lower right is the corrected gravity anomaly.

2.3 Reference Earth models

In addition to the corrected gravity data set as a constraining input to our joint inversion schemes for MT data (JI2), we use two different physical parameter models as inversion constraints: a 3D regional density model by Maystrenko et al. (2013) for JI1, and a local 2D seismic velocity model along profile 100 acquired as part of the SAMPLE project (Fromm et al., 2017; Fromm et al., 2015) for JI3.

The density model is based on a forward modeling study of 3D gravity satellite data and encompasses a much larger domain than considered in our study. We only use the northern part intersecting with our inversion model. The model has been derived conducting gravity and

thermal modeling and inclusion of 2D seismic profiles that were available in the region at the time. It comprises constant regions with different density values representing, in addition to water and air, 10 different geological units including five sediment- and four crustal units as well as the lithospheric mantle. We extrapolated the density model by Maystrenko et al. (2013) to the North-west and interpolated it onto our inversion grid so it can be used as a constraint in the MT inversion. The identified geological features as well as the geological inferences from the seismic data in our region of interest are described in more detail in the discussion section. As the regional 3D density model is characterized by discrete densities for the different geological units it provides structural constraints for the inversion of the Earth model. Therefore, we refer to it as the 3D structural density model.

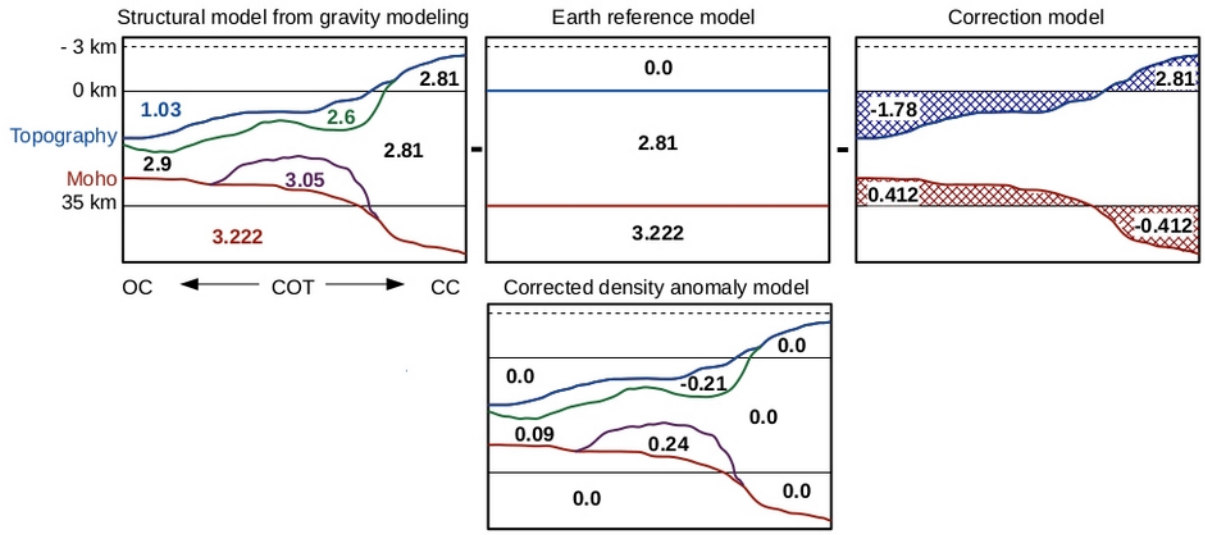

Figure 4. Concept for the density starting model corrections. The top panel shows sketches of vertical profiles crossing the continent ocean transition (COT) from oceanic- (OC) to continental crust (CC) of the structural model derived from Maystrenko et al (2013), a simple, layered reference earth model, and the correction model used for data corrections. The lower panel is a sketch of a vertical profile through the density anomaly model for the inversion input.

In contrast to the structural density model we also examined a gradient velocity model as an inversion constraint. Since no 3D velocity model is available in the region, we had to use a local 2D velocity model. We chose the 2D velocity model along profile 100 (and Walvis Ridge)

derived by Fromm et al. (2017), which had been generated through forward modeling of refraction and reflection data. The model is characterized by layers or blocks with downward-increasing velocity gradients, leading to some strong gradients at layer boundaries and gentler gradients within the layers.

To account for the dimensionality difference of the described 2D seismic reference model and the 3D character of our MT data, we performed a 3D joint inversion (JI3) on a narrow cube around the profile (which we consider as "quasi-2D" from now on). We chose a model width of 40 km in strike direction of profile 100 to limit the model to the expected extent of the anomalous crustal structure beneath Walvis Ridge. To build the inversion constraint-model, the reference velocity model was interpolated along the profile onto the main inversion grid and extended left and right of the profile, to fit the 40 km wide 3D model. For the coast parallel profile 3, the strong resistivity variations caused by the coastal resistivity transition cannot be included in a narrow model. Therefore a "quasi-2D" inversion cannot be performed satisfactorily along that profile.

3 Joint Inversion Scheme

We used jif3D framework for the joint inversion (Moorkamp et al., 2011). It includes a 3D MT integral equation forward engine developed by Avdeev et al. (1997), an internally developed voxel based full tensor gravity forward engine (Moorkamp et al., 2010), and a 3D seismic first arrival refraction code (Heincke et al., 2017; Podvin & Lecomte, 1991). However, since no 3D seismic data are available, we did not activate the seismic modeling option. The framework allows the implementation of a parameter relationship or a structural cross-gradient coupling. The results presented in this paper are based on a structural coupling approach because of the lack of commonly valid parameter relationships for the various lithologies found in the study area.

Equation 1 denotes the full objective function which is minimized iteratively using a limited memory quasi-Newton scheme (L-BFGS) (e.g., Avdeeva & Avdeev, 2006; Nocedal & Wright, 2006):

$$\phi(m) = w_{MT}\,\phi_{dMT}(m) + w_{Grav}\,\phi_{dGrav}(m) + \lambda_{MT}\,\phi_{RegMT}(m) + \lambda_{Grav}\,\phi_{RegGrav}(m) + \kappa\,\phi_{Cross} \qquad (1)$$

The objective function includes the RMS data misfit terms for the MT and gravity data (Φ_{dMT} and Φ_{dGrav} respectively) and measures for the roughness of the physical parameter models (Φ_{RegMT} and $\Phi_{RegGrav}$). These regularization terms are included in the objective function to attain smooth models by minimizing parameter variations in neighboring cells, and stabilize the iterative inversion procedure. Coupling between different physical parameter models is implemented through a structural coupling term Φ_{Cross}, consisting of the cross-gradient of the two different physical parameter models under consideration (Gallardo & Meju, 2003). Cross-gradient coupling has proven to be a powerful tool for coupling in joint inversion in synthetic- as well as real data-studies (e.g., Colombo & Rovetta, 2018; Um et al., 2014; Zhou et al., 2015). The cross-gradient coupling enforces spatial resemblance of the inversion model with the reference model. This type of coupling is rather loose, as the parameter gradients of the inversion and reference model can point in either the same, or opposite direction to obtain a minimum value for Φ_{Cross}. Furthermore, it is zero, when either of the gradients is zero.

The data misfit, regularization-, and cross-gradient terms in the objective function are weighted with Lagrange multipliers. We employ a cooling strategy for the two regularization weights λ_{MT} and λ_{Grav}, which recovers large-scale structures first and then allows for smaller-scale model variations by subsequently reducing the weights (Moorkamp et al., 2020). A setup with initial small regularization weights results in rough models with large parameter jumps and large regularization- and cross-gradient terms. In the joint data inversion approach (JI2), the MT data misfit term is weighted stronger with a larger w_{MT} than the gravity data misfit term, because its optimization requires many more iterations than the gravity data optimization. Cross-Gradient weight κ is kept high to ensure a strong coupling between the MT inversion and the gravity data or reference model constraints. Specific Lagrange multipliers chosen for JI1, JI2 and JI3 are listed in Table 1.

The inversion model grid consists of 96 x 96 x 34 cells. Horizontal cell sizes are uniformly 10 x 10 km, vertical cell sizes increase from 300 m to 50 km in order to adapt to decreasing sensitivity with depth yet allow for a sufficiently close fit of the topography. We used the ETOPO 1 Global Relief Model to constrain the water depth within the model area (Amante & Eakins, 2009). The integral equation MT modeling code requires a background model. We chose 4 layers overlying a half-space representing the air, ocean, sediment, crust and mantle layers. The lower layer boundaries were set to -0.9 km, 3 km, 7 km, 65.5 km and the respective

electrical resistivities to 100000 Ωm, 0.3 Ωm, 1 Ωm, 50 Ωm, and a 10 Ωm half-space below. These values are intended to represent the average surrounding resistivity structure. This cannot adequately account for the resistivity variations of adjacent crustal domains, i.e. oceanic crust to the west and north of Walvis Ridge, continental crust to the east and thickened magmatic crust to the south. To reduce the influence of the background model, we increase the lateral extent of our model by 250 km beyond the region covered by the MT stations.

The resistivity starting model is chosen to resemble the setup used for the previous inversion in Jegen et al. (2016). It includes a sediment layer with thicknesses taken from Maystrenko et al. (2013) and an electrical resistivity of 1 Ωm. This is underlain by a homogeneous half-space with an electrical resistivity of 50 Ωm. Salt water resistivities are set to 0.3 Ωm. To test the influence of the starting model on our joint inversions, we also performed inversions with a pre-fitted resistivity model. This pre-fitted starting model is the inversion model resulting from an MT-only inversion with high regularization after 75 iterations. At this point the RMS MT data misfit is reduced from 6.55 to 3.92. The resulting model includes increased mid-crustal resistivities and distinct shallow conductive basins, instead of a simple sediment layer. In the joint inversion with gravity data (JI2), this pre-fitted resistivity starting model seems to have no significant effect on the final inversion results. However, for joint inversion approaches JI1 and JI3, the starting models seems too specific causing large values in the cross coupling term that subsequent inversion iterations cannot reduce. Hence, we computed the final inversions shown here with the half-space resistivity starting model described above, to allow the most flexible inversion convergence. Model parameters of the ocean layer and bathymetric variations were fixed during the inversion.

The density starting model for JI2, i.e. the full joint inversion of both datasets, requires more structure than the resistivity starting model, because gravity inversion alone has no depth sensitivity. We created an initial model with large-scale structures based on the density model by Maystrenko et al. (2013) (Fig. 4, top left). Absolute densities were converted to density anomalies by subtracting a very simple earth reference model (Fig. 4, top center). This reference model consists of three layers representing air (above 0 km; 0 kg/m^3), crust (0 - 35 km; 2.81 kg/m^3), and mantle (below 35 km; 3.222 kg/m^3). Afterwards, the previously described data correction models for topography- and Moho depth variation (Fig. 4, top right) were subtracted to account for the corrections applied to the gravity data. This correction corresponds to a

flattening of the surface and Moho topography in the model to the reference levels of 0 km and 35 km, respectively. Comparing our density starting model to the earth reference model (Fig. 4, top center) the main features are characterized by: a) reduced density at shallow depths indicating sediments, b) slightly increased density for oceanic crust, and c) a density increase for the proposed magmatic underplating.

4 Results

We compare the 3D MT data inversion to three different joint inversions: In JI1 we use the structural density model as an external constraint to MT data inversion, in JI2 we apply a joint inversion of the MT-, and corrected gravity data with the resistivity-, and density starting model described in the previous section and in JI3 we perform a quasi 2D inversion of the MT data along Walvis Ridge with a 2D gradient velocity model from the congruent seismic data set as a constraint. In the comparison and analysis of our inversion results we consider three aspects. First, we examine the influence of the chosen weighting parameters and the development of the different objective function terms. Second, we compare the data misfits which are achieved by the inversions in detail. Third, we compare the resulting physical parameter models highlighting differences emerging from the different coupling strategies, and analyze these features further with a sensitivity analysis.

4.1 Weighting parameters and misfit evolution

Inversion progress is heavily steered by the weighting parameters (w_{MT}, w_{Grav}, λ_{MT} , λ_{Grav}, and κ), which drive inversion convergence. For our analysis, we monitor the development of the different misfit terms: MT and gravity data misfits $\Phi_{d(MT/Grav)}$, MT and gravity regularization $\Phi_{Reg(MT/Grav)}$, and cross-gradient coupling Φ_{Cross} (see Eq. 1). Due to the nature of the calculation of the misfit terms (see Moorkamp et al., 2011), the values differ by orders of magnitude, and require weights to be set in order to achieve a balance of the terms in the objective function. The applied weights are summarized in Table 1, the evolution of each term is shown in Figure 5. Please note that values shown for data misfits in Figure 5a are not weighted by Lagrangian parameters. Therefore, values approaching a value of one indicate a fit of the modeled and observed response within the assumed data errors.

For the MT-only and model constrained approaches JI1 and JI3, only the MT data set is inverted, therefore w_{MT}=1 and w_{Grav}=0. In the joint data inversion approach (JI2), the two data sets are weighted differently to account for the much slower convergence of MT- compared to gravity inversion. After testing different ways to balance both data sets, the best results were achieved by using weights w_{MT}=50 and w_{Grav}=1. Smaller w_{MT} values lead to a fast fit of the gravity data, while MT data cannot be fitted well. The joint inversions were stopped when the MT data misfit had reached the single-method MT data misfit (3.01 for JI1 & JI2, 3.84 for JI3). All data misfits (Fig. 5a) experienced an initial drop and decrease more moderately afterwards. The two model-constrained approaches (JI1 and JI3 corresponding to the green and orange line in Fig. 5) required distinctly more iterations than the MT-only and joint data inversion (JI2). This implies that using cross-gradient coupling with a fixed model strongly reduces the speed of inversion convergence.

For regularization weights λ_{MT} and λ_{Grav}, we implement a cooling scheme, starting with high values and successively reducing them (see Table 1) after each 75 iterations. The specific regularization weights are chosen to achieve an optimal balance between computation time and efficient convergence. However, optimization is stopped automatically before, if no suitable step size can be found to significantly minimize the objective function with the L-BFGS method (Avdeev & Avdeeva, 2009; Tarantola, 2005). Once the final weights λ_{MT} and λ_{Grav} are reached, the inversion continues as long as the value of the objective function can be further reduced or the target RMS is reached. The regularization terms of the objective function show, just like the data misfit, an initial decrease that we can attribute to the initial smoothing of sharp boundaries in the starting models (Fig. 5b). Afterwards, the regularization terms further decrease due to the cooling scheme, but then they slightly increase as models develop more distinct and smaller-scale features resulting in increased model roughness.

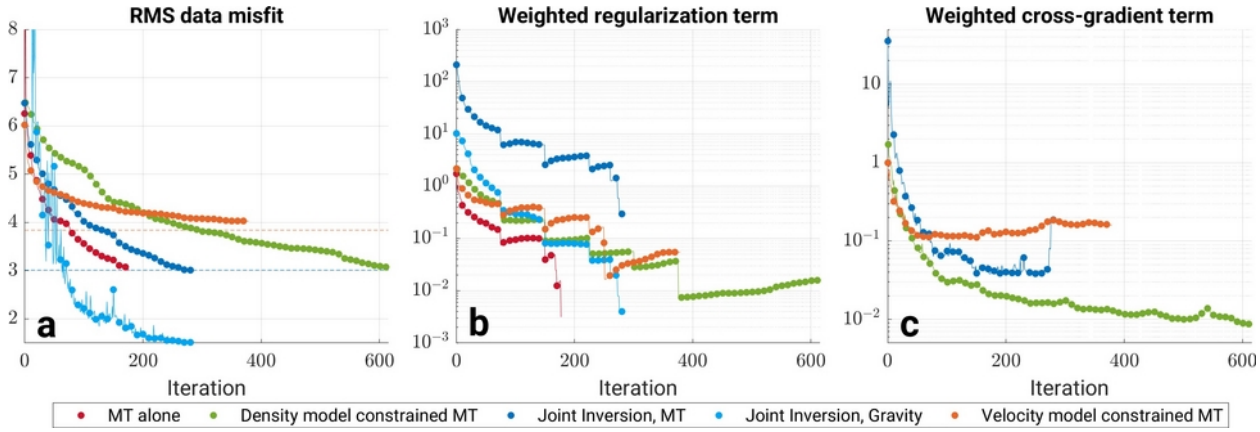

Figure 5. Development of a) data-, b) regularization-, and c) cross-gradient coupling terms during the inversion iterations for all four inversion approaches. In a) the overall-model's RMS misfit is depicted. The dotted lines indicate the target RMS misfit for the full 3D (red, green, blue) and the "quasi-2D" (orange) inversions. This is the final value reached by the single-method MT inversions. In b), the regularization terms Φ_{RegMT} and $\Phi_{RegGrav}$ are weighted with their Lagrange multipliers λ_{MT} and λ_{Grav}. In c) the coupling terms Φ_{Cross} are weighted with the Lagrange multiplier κ. Red is the single-method MT inversion, green is JI1, both blue colors are JI2 (MT and Gravity method), and orange is JI3.

The cross-gradient coupling weight κ was kept high during inversion to ensure a strong influence of cross-model coupling and balance the term Φ_{Cross} with respect to the data misfit. The coupling terms Φ_{Cross} show a fast initial drop and then smaller decreases for JI1 and JI2 (Fig. 5c). While at larger iteration numbers, the inversion still alters the models to decrease the data misfit, the coupling term in the objective function does not change significantly any more. This can either indicate that model gradients are unified, and structural similarity is achieved (ideally), or that resistivity model changes are focused mainly inside constant features of the cross-model (i.e. for the density model constrained approach JI1). For the cross-gradient coupling with the 2D velocity-model (JI3), the cross-coupling term increased beyond iteration 250 (orange line in Fig. 5c). At this point, the MT data misfit could only be improved by allowing for more structural dissimilarity between the resistivity model and the velocity model.

Increasing the coupling weight κ during the final iterations of JI2 (blue line, Fig. 5c) does not change the MT data misfit but enabled can us to decrease the regularization weights λ_{MT} and

485 λ_{Grav} further without an otherwise strong increase in the coupling term Φ_{Cross}. This shows that the
486 joint inversion is at least partly sensitive to the coupling weight κ.

487 Table 1. Inversion Weighting Parameters and Final Data Misfit for all four Inversion Approaches

	MT data weight w_{MT}	Gravity data weight w_{Grav}	MT regularization weight λ_{MT}		Gravity regularization weight λ_{Grav}		Coupling weight κ	Number of iterations	Final MT data RMS	Finale Gravity data RMS
			start	end	start	end				
MT-only	1	-	100	1	-	-	-	178	3.01	-
Density model constrained MT (JI1)	1	-	100	1	-	-	10000	611	3.07	-
Joint MT and Gravity (JI2)	50	1	10000	100	1000	10	100000-500000	283	3.01	1.52
Velocity model constrained MT (JI3)	1	-	100	1	-	-	100000	380	4.03	-

488

489 In summary, we observe that all terms in the objective function show initial strong drops,
490 caused by fitting of the inversion models to main data anomalies, and smoothing of the abrupt
491 starting model boundaries. Also, the two model-constrained approaches (JI1 and JI3) converge
492 much slower compared to the MT alone and joint data inversions (JI2). The reason for this
493 reduced inversion speed is that in model-constrained joint inversion approaches only the
494 resistivity model is altered. Yet, one more term in the objective functions (Φ_{Cross}) has to be
495 minimized compared to a single-method inversion. In joint data inversion (JI2), two models can
496 be modified in order to satisfy the different objective function terms. Lastly, we find that the
497 regularization terms' behavior is strongly dependent on the corresponding weights. As we use a
498 cooling strategy for λ_{MT} and λ_{Grav}, misfits Φ_{RegMT} and $\Phi_{RegGrav}$ may increase, however, the weighted
499 misfits decrease (Figure 5b).

4.2 Data fit of the resulting inversion models

Depicting MT data as pseudo-sections is an easy way to get a first overview of possible resistivity structures. Apparent resistivities ρ_a can be calculated directly from the impedance matrix elements and plotted against period as an indirect measure for depth. Figure 6 shows pseudo-sections for the XY element of the observed apparent resistivity ρ_a in direct comparison to the final model responses achieved by our four inversion approaches as a first evaluation of the achieved data fit. The observed data (top row, Fig. 6) show low apparent resistivity anomalies in the short periods (especially stations 13 – 19 and 25 – 30), which are well represented in all modeled apparent resistivity data (rows 2 to 4 in Fig. 6). The models also account for the high apparent resistivity anomalies at intermediate periods (especially stations 3 – 13 and 33 – 43), yet none of the four inversion approaches matches its full extent. For the onshore stations (right column, Fig. 6), the observed apparent resistivities show large variations between neighboring stations 100 to 120, which are located along a coast-parallel profile with distances of around 20 km. The inversions do not result in similarly varying apparent resistivities.

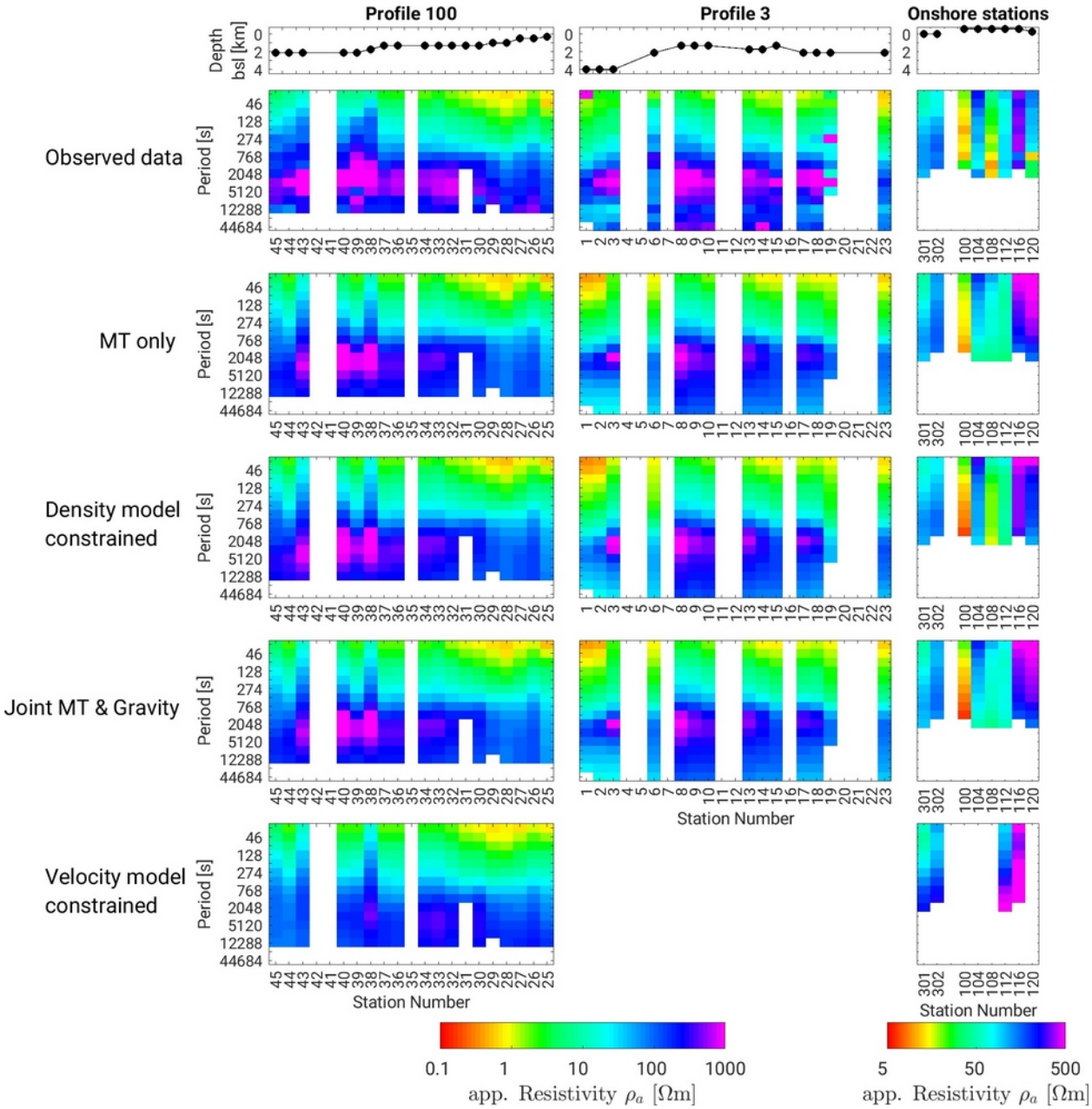

Figure 6. Pseudo-sections of the XY component of apparent resistivity ρ_a. Top row: Position of MT stations along the two profiles and land stations. Row 2: Pseudo-sections for the observed data. Rows 3 to 6: Model response of all four inversion approaches. Row 2 is the MT-only responses, row 3 is JI1, row 4 is JI2, and row5 is JI3. Left column, profile 100 along Walvis Ridge; middle column, profile 3 parallel to the coast; right column, onshore stations.

To further evaluate the data fit of the final four resistivity models, we compare the root mean square (RMS) misfit of the impedance matrix Z (Eq. 2, misfit calculated separately for each frequency and station). This misfit denotes the difference between a measured (Z^{obs}) and a calculated (Z^{syn}) parameter and is weighted by the parameter error Z^{err}.

$$RMS = \sqrt{\frac{1}{8}\sum_{k}\left[\left(\Re\left(\frac{Z_k^{syn}-Z_k^{obs}}{Z_k^{err}}\right)\right)^2+\left(\Im\left(\frac{Z_k^{syn}-Z_k^{obs}}{Z_k^{err}}\right)\right)^2\right]} \qquad \text{with k=\{XX,XY,YX,YY\}} \qquad (2)$$

The final overall RMS data misfits (averaged over all frequencies and stations) are stated for all models in Table 1. In Figure 7, we show the RMS data misfits for each MT station and each frequency together with the mean impedance element's error Z^{err} of Equation 2. This depiction allows to analyze where our resistivity model cannot explain the measured data well and hence the results should be interpreted cautiously. Several land stations show poor fits in all inversion approaches, while the corresponding impedance errors are high. These poor fits emphasize the difficulty to identify complex onshore resistivity structures (see Kapinos et al., 2016) with few MT stations and indicate the presence of noise in the onshore data measurements. The outer stations of offshore profile 3 (stations 1-3, 23) mostly have RMS misfits above 4, while having very low impedance errors. Stations 1 to 3 are located just north of the Florianopolis Fracture Zone that marks a change of thick crust below the Walvis Ridge to thin crust in the Angola Basin. The southern-most station 23 is isolated due to data loss on stations 20 to 22 and situated close to supposedly deep sedimentary basins (Maystrenko et al., 2013; Stewart et al., 2000). The high RMS data misfits are a first indication for complex resistivity structure at depth that may not be sufficiently resolved by the data coverage and model scope. Thus, the inversion results for the areas around the Florianopolis Fraction Zone, in the southern part of the study area, and onshore have to be interpreted with care.

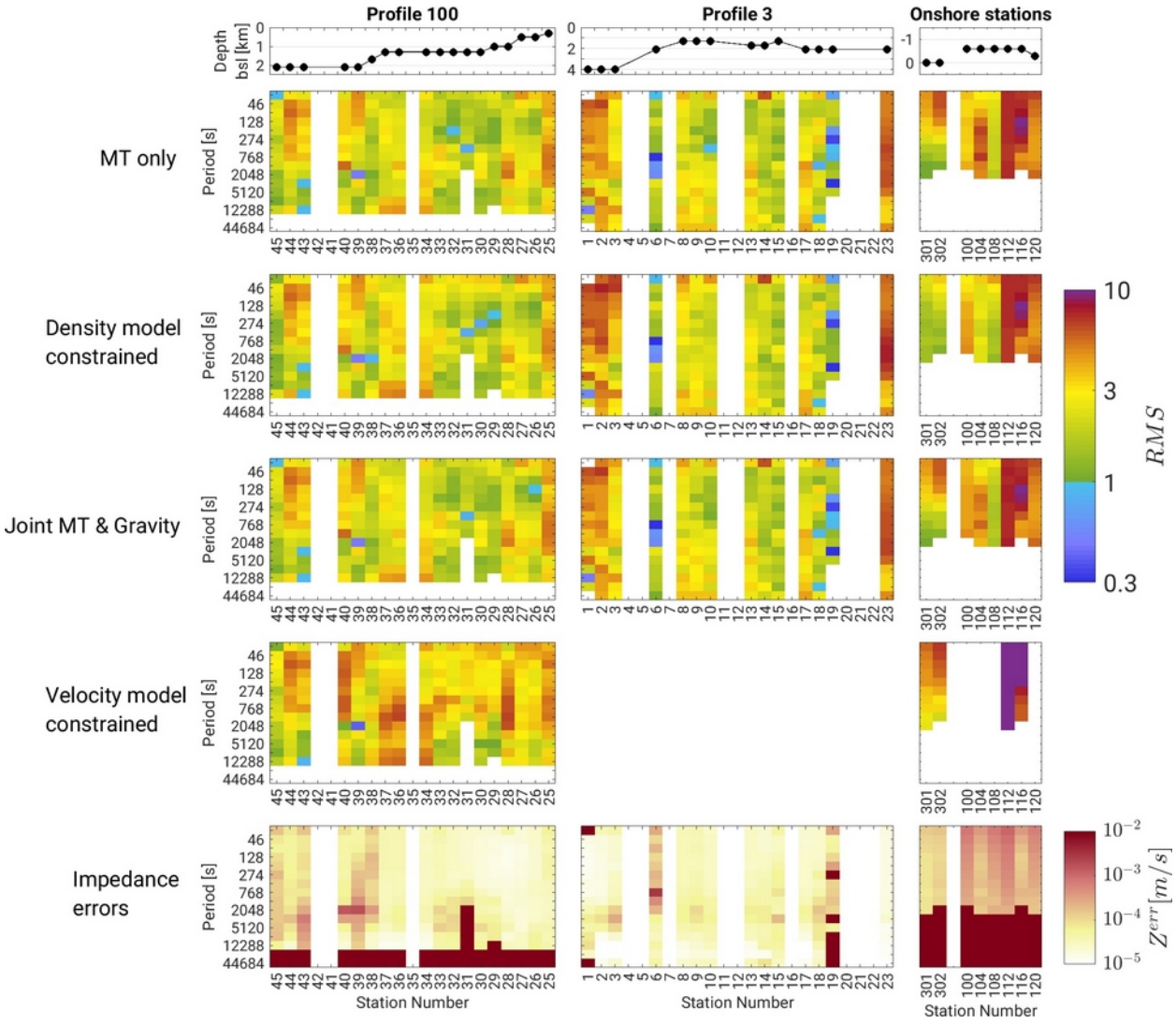

Figure 7. Pseudo-sections of MT data RMS misfits (Eq. 2). Top row: Position of MT stations along the two profiles and land stations. Row 2 to 5: Final MT data RMS misfit for each station and each frequency for the four inversion approaches (MT-only, JI1, JI2, JI3, respectively). Blue colors indicate overfitting. Bottom row: Impedance matrix errors Z^{err} for all MT stations.

The gravity data's final RMS misfit in the joint data inversion (JI2) is highly dependent on the coupling weight κ. A weak coupling constraint allows for a free fit of the density model. In the joint inversions, we vary κ between 10000 and 500000, reaching gravity data RMS between 1.4 and 3.7, while gravity inversion alone reaches an RMS of 1 (i.e. ideal fit) after ~200 iterations. The spatial variation of gravity data misfit is shown in Figure 8. The largest

differences occur at the abrupt bathymetry changes along the Florianopolis Fracture Zone and the landfall of Walvis Ridge. Residuals from gravity modeling by Maystrenko et al. (2013) show similar patterns, i.e. high residuals are observed in the same region, and positive and negative residual anomalies occur next to each other. Rapidly changing crustal composition, small-scale seamounts, or sedimentary depocentres together with insufficiently resolved bathymetry variations can all be potential reasons for these increased data residuals. Neither a reduction of the gravity inversion cell size, nor an unconstrained gravity inversion of a half-space fully his pattern.

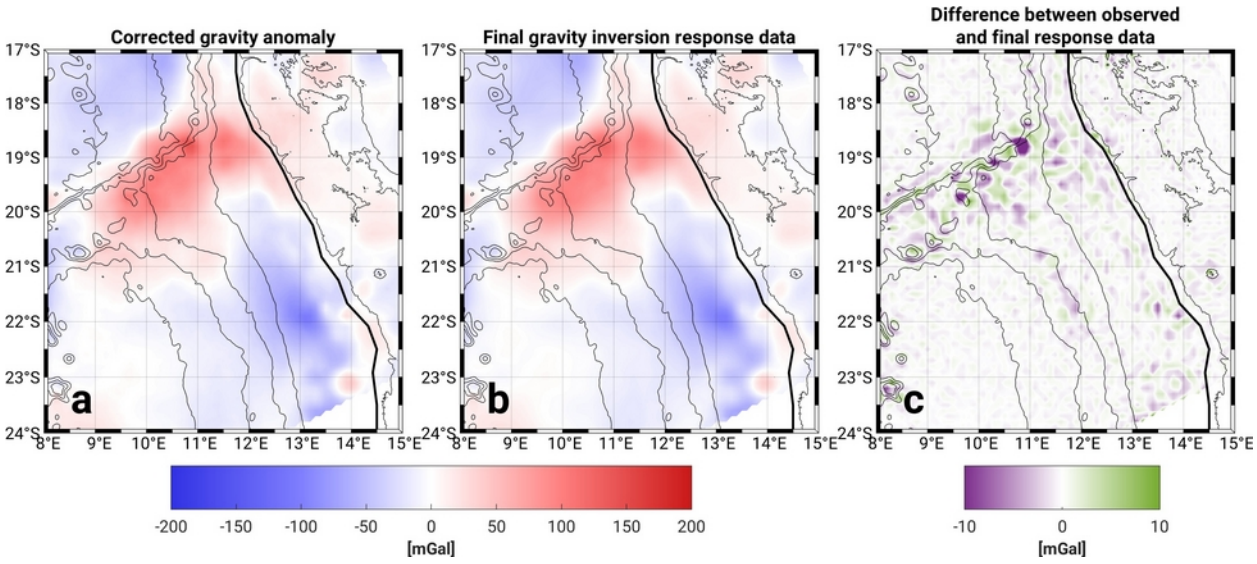

Figure 8. Map views of gravity data and residuals of JI2. a: bathymetry and Moho depth corrected gravity anomaly (inversion input data). b: gravity anomaly response for the final inversion density anomaly model. c: difference between observed (a) and final response (c) data i.e. gravity residual.

In summary, the inversions reach satisfactory data fits and are capable of resolving large-scale variations indicated by the apparent resistivity pseudo-sections. Larger MT data misfits are concentrated at the outer parts of profile 3 and the land stations, which indicates model uncertainties in these regions. The largest gravity data misfits are located at the landfall of Walvis Ridge and most likely correspond to short-wavelength gravity features generated by local density variations which are not resolved by our density model and the available bathymetry.

4.3 Model comparison

To compare the four resulting inversion models, we present vertical slices along profiles 100 and 3 through all final physical models (Figures 9 & 10). The vertical slices are chosen to lie right underneath the MT stations, where the resistivity models are best constrained by the MT data. Figure 9 shows final resistivity models along profile 100 for all four approaches, i.e. MT-only and JI1, JI2 and JI3 on the left column. In the right column we depict the corresponding slice of the structural density model (JI1) used to constrain our MT data inversion, the final density model from the joint data inversion approach (JI2) and the velocity model (JI3) along the profile that strikes along Walvis Ridge that constrained our MT inversion. Figure 10 shows the corresponding results for Profile 3 except for JI3 which could not be performed on this profile. For better comparability with the cross-model of JI1, we transform the density anomaly model of JI2 back to absolute densities by adding the reference and the correction model to the inversion result, i.e. reverse to what is described in Figure 4. To compare the three-dimensional extent of structural features, we show horizontal slices through the final 3D resistivity models at 25 km depth and the corresponding horizontal slices of the structural density model and the density model derived from the joint MT gravity data inversion (Fig. 11). We focus our discussion on the most prominent three features in terms of size and resistivity contrast. These features are the shallow conductors corresponding to sediments (e.g. C2 & C3 in Fig. 9 & 10), the large resistor at intermediate depths associated with magmatic underplating (R in Fig. 9, 10, & 11) and a deep, narrow conductor on profile 3 around kilometer 90 (C1 in Fig. 10 & 11) in the vicinity of the Florianopolis Fracture Zone.

Prominent shallow, low-resistivity features associated with marine sedimentary basins occur in the same locations in all four inversion models, while some vary in thickness. Along profile 100 (Fig. 9) two wide basins dominate from profile kilometers ~20-100 and ~220-380 (anomaly C2). On profile 3 (Fig. 10) a more continuous, upper, conductive layer with several incisions (anomaly C3) is visible in the resistivity models. The low-resisivity sediments reach thicknesses of about 8-10 km in the MT-only resistivity models. In the joint inversion resistivity model (JI2) depicted in Figures 9 and 10d, these conductors are almost identical to the MT-only model with a slight conductivity increase (i.e. basin at kilometer 150 on P100). In the corresponding density model (Fig. 9 and 10e), low density anomalies are observed analogue to the conductivity anomalies. For the two model-constrained approaches JI1 and JI3 (Fig. 9b & f

and Fig. 10b), the sediments have more shallow lower boundaries (e.g. anomaly C2 on profile 100 at ~ 3-5 km depth) due to the cross-models' strong vertical gradients from sediments to upper crust.

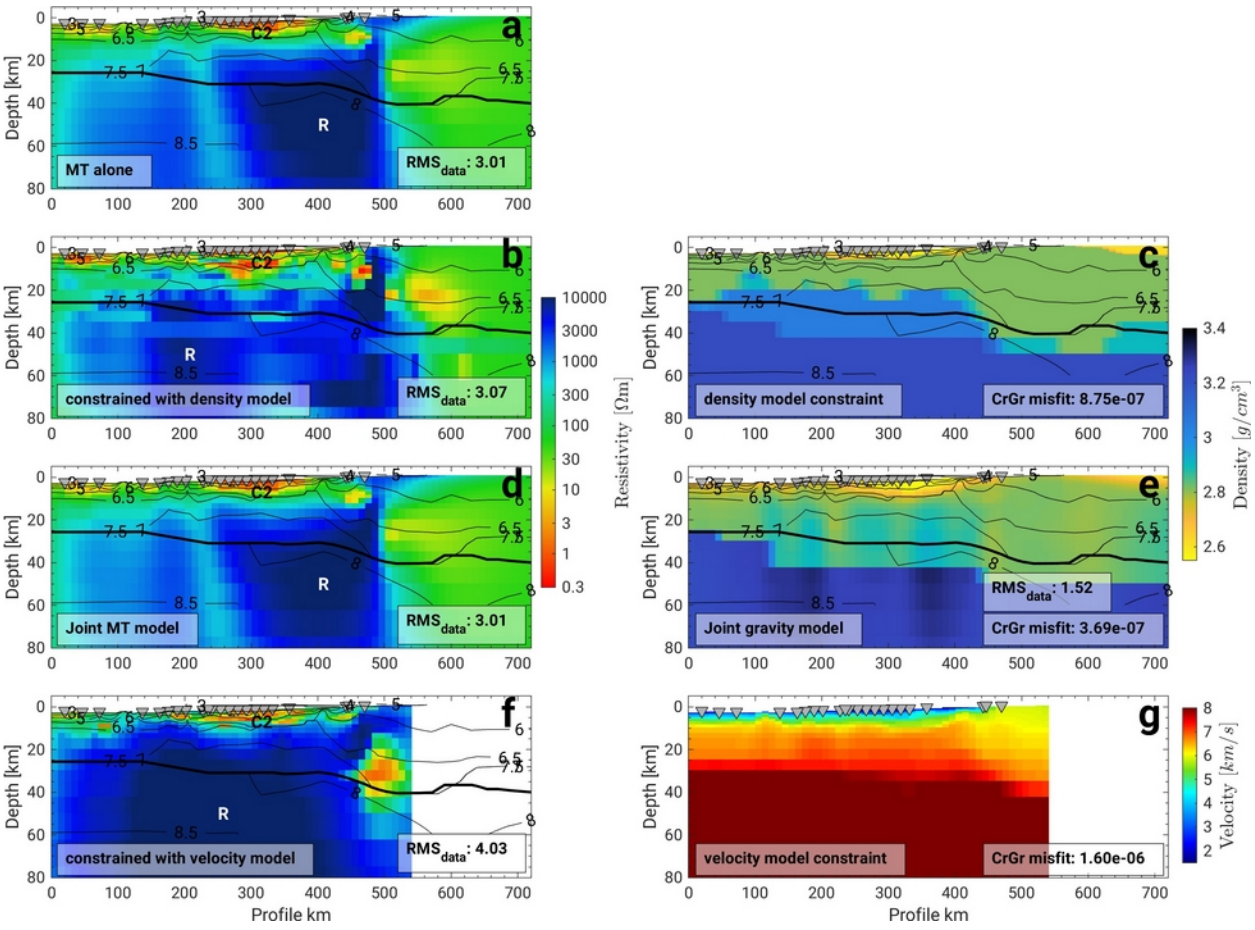

Figure 9. Vertical slices through physical inversion models along profile 100. Shown are the final resistivity models for all four approaches (a) MT-only, b) JI1, d) JI2, f) JI3) on the left with the according cross-models (density and velocity) on the right. Black lines on top are seismic velocities from Fromm et al. (2017), with the thick line representing the Moho as the 7.8 km/s isoline. Anomaly R presents the large mid-to-lower crustal resistor associated to magmatic underplating. Conductor C2 images a sedimentary basin. Overall RMS data misfits as well as summed cross-gradient coupling terms are shown in the white boxes. Grey triangles denote the positions of MT stations.

We conduct sensitivity tests by varying the feature's resistivity values and extent to investigate the resolution capabilities of the sediment layers in our inversion models on one hand and to examine the nature of the described shallow boundaries introduced from the structural density and velocity constraint-models on the other hand. The sensitivity test models were produced by altering the final MT-only inversion resistivity model based on the model differences indicated from our added constraints. Forward calculations of these models allow us to observe the influence of structural- or parameter changes on the MT data fit. The final MT-only inversion model was modified, by a) increasing sediment resistivities (the resistivity in every cell with a resistivity below 12.5 Ωm is doubled) to challenge the need for shallow conductors; b) decreasing sediment thickness (cells with resistivity below 12.5 Ωm are averaged over a vertical window of 5 cells, which increases those values but ensures smooth gradients) to test whether thinner conductors could fit the MT data; and c) reducing the sediment thickness by about a factor of 2 while simultaneously decreasing it's resistivity to ensure a constant conductivity-thickness ratio (conductance). Exemplary slices through the inversion- and test models along P100 are shown in Figure 12 alongside the response data for station 28 on this profile. Changing the sediments in the resistivity model changes the response in all four components emphasizing the 3D-effect of the sediment distribution. The response curves of test a) deviate significantly from the observations, which implies that generally shallow low resistivity values are needed to fit the data. While the curves of test b) seem close to the response of the inversion result for this specific station, the overall RMS (summed over all stations) of 9.5 shows an insufficient data fit. Test c) shows that the test model's responses are very close to the inversion model response. It emphasizes the MT method's sensitivity to conductance and its incapability to resolve both conductivity and thickness, particularly for shallow structures. For this test, we continue the inversion for 20 iterations after which data misfits are reduced to fit the original MT-only inversion RMS of 3.01, while the altered shallow conductors remain thinned and less resistive.

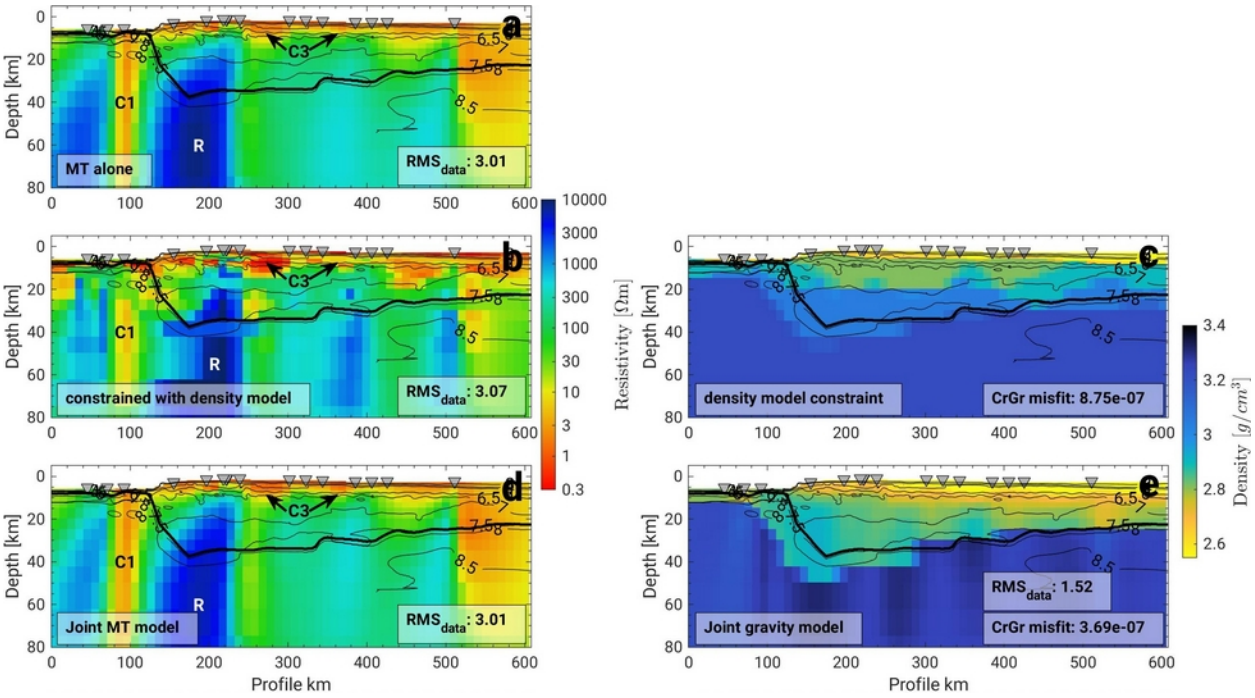

Figure 10. Vertical slices through physical inversion models along profile 3. Shown are the final resistivity models for the three 3D approaches (a) MT-only, b) JI1, d) JI2) on the left with the according density cross-models on the right. Black lines on top are seismic velocities from Planert et al. (2016), with the thick line representing the Moho as the 7.8 km/s isoline. Anomaly R presents the large mid-to-lower crustal resistor associated to magmatic underplating. Conductor C1 coincides with the Florianopolis Fracture Zone and conductor C3 matches seismic observations of seaward dipping reflections. Overall RMS data misfits as well as summed cross-gradient coupling terms are shown in the white boxes. Grey triangles denote the positions of MT stations.

Most eminent in all inversion models is the large, high resistivity body R from about 16 km depth downward, stretching from the coast seawards along Walvis Ridge. While the resistor seems continuous with depth and also laterally apart from the decrease in resistivity around profile kilometer 220 in profile 100, it becomes discontinuous in the structural density model constrained joint inversion JI1. The boundaries of these discontinuities coincide with the strong parameter gradients in the cross-model at the top (~19 km) and bottom (~42 km) of the high density lower crustal body (2.95 kg/m³) ascribed to magmatic underplating in the structural density model. The resistor's lateral extent along the off-profile-axis in this density-constrained resistivity model of JI1 is furthermore limited to areas close to MT stations, while it stretches

660 over the adjoining areas in all other inversion models (Fig. 11 b). While the strong resistivity
661 contrast marking the transition from continental crust to magmatically-imprinted oceanic crust
662 directly at the ridge's landfall remains, the highest resistivities in the density-constrained model
663 are focused more seawards around 200 km on profile 100. In contrast, the MT-only inversion
664 resistivity model has the highest values at kilometers 300-500 (comparison of Fig. 9a & b). The
665 joint inversion JI2 resistivity model (Fig. 9 & 10d) shows a smooth resistor, almost identical to
666 the MT-only approach. In this inversion, the distinct initial high-density body just below Walvis
667 Ridge is smoothed out vertically (Fig. 9 & 10e). Increased densities are still focused below the
668 ridge, but cover a larger depth range reaching below the Moho. The MT-only, JI1, and JI2
669 models show a decrease of resistivity around depths of 80-100 km (visible at the very bottom of
670 Fig. 9 & 10 a, b, d). However, they show no marked decrease in resistivity at Moho depths.
671 Lastly, in the velocity-constrained resistivity model along Walvis Ridge (Fig. 9f), the resistor is,
672 compared to the MT-only and JI2 model, laterally smoother and the most resistive part is shifted
673 seawards. This resistor matches the lower crustal high velocities stretching over a wide area from
674 profile kilometer 130-470 (Fig. 9 g). The velocity-constrained resistivity model (Fig. 9f)
675 indicates no resistivity change at Moho depths and no resistivity decrease at the bottom of the
676 model.

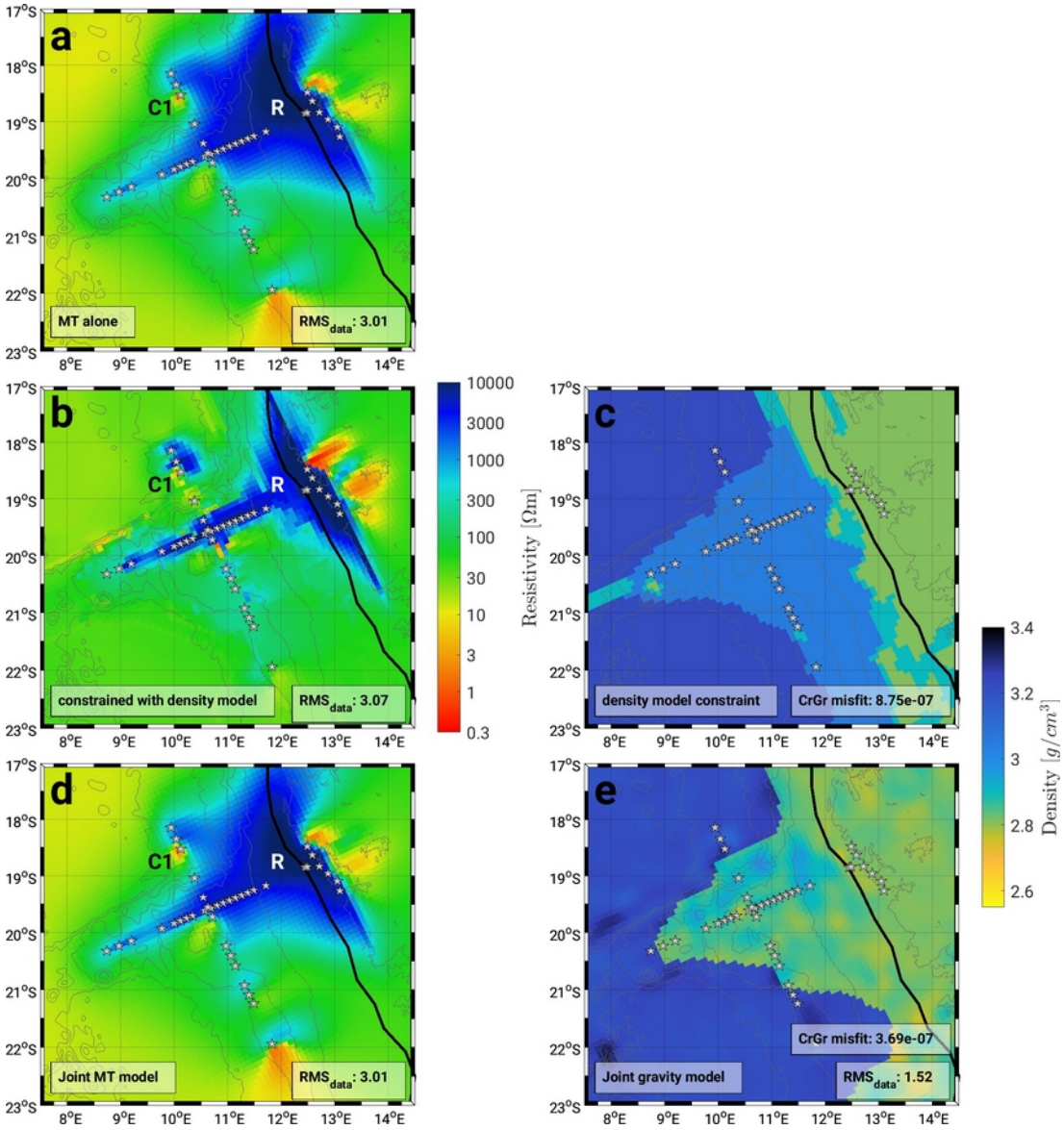

Figure 11. Horizontal slices through the physical inversion models at 25 km depth. Shown are the final resistivity models for the three 3D approaches (a) MT-only, b) JI1, d) JI2) on the left with the according density cross-models on the right. Anomaly R presents the large mid-to-lower crustal resistor associated to magmatic underplating. Conductor C1 coincides the Florianopolis fracture zone. Overall RMS data misfits as well as summed cross-gradient coupling terms are shown in the white boxes. Grey stars denote the positions of MT stations, grey lines are bathymetry.

We conducted tests to examine how much the form of this high-resistivity body could be changed without influencing the response data and thus the data misfit. The tests we conducted

686 are: d) reducing the resistive feature's thickness and simultaneously increasing its resistivity to
687 check to which degree its thickness can be reduced to match the cross models'; e) removing the
688 resistor anomaly north-east of the profile intersection by reducing the highest resistivities; and f)
689 removing the resistor anomaly south-east of the profile intersection. Compressing the resistor to
690 a thinner, more resistive anomaly (test d) has a strong impact on the MT response curves. We
691 test for different thicknesses (30 – 100 km) and increase the feature's resistivity step-wise up to
692 10 times the original value. It is not possible to fit the curves and achieve similar data misfits. In
693 order to decrease the misfit to the original level, the high-resistivity anomaly is always enlarged
694 towards the model's lower boundary. Therefore, it appears, that high-resistivity values need to
695 reach deep (at least 80-100 km) into the Earth's mantle to explain the data and we do not expect
696 a drastic change of resistivity at Moho depth. Tests e) and f) challenge the reduced off-axis
697 extent of the resistor indicated by the JI1 resistivity model (Fig. 11b). They indicate the limited
698 horizontal resolution away from the MT stations. If values in close proximity (~ 30 km away
699 from the stations) are kept constant, changes of resistivity affect the response curves only
700 marginally. Therefore, this test emphasizes that MT inversion results far from stations have to be
701 interpreted with great care as the results may be driven mostly by smoothing or the influence of
702 the 1D background model. Therefore, it is likely that strong additional constraints can alter the
703 resistivity model in area's far away from MT stations relatively freely, meaning interpretation of
704 such features would rely mostly on the credibility of the constraining cross-model or data.
705 Additionally, to the described sensitivity tests d) to f), we also estimate the inversion's
706 responsiveness to the distinction between the highest resistivity values (i.e. differentiation
707 between 2000 Ωm and 10000 Ωm). It shows that values above 2000 Ωm are only barely
708 distinguishable, as the response curves do not change substantially, when confining resistivities
709 to a maximum of 2000 Ωm. Therefore, we do not interpret variations in resistivity that occur
710 within the highly resistive regions of our model.

711 The third prominent feature in the inverted resistivity models, is the deep, narrow low-
712 resistivity anomaly on profile 3 at ~90 km and below station 3 at ~10.1°E, 18.5°S (Fig. 10 & 11,
713 anomaly C1). This anomaly could be related to the Florianopolis Fracture Zone marking the
714 northern edge of Walvis Ridge (cp. Fig. 1). Water intrusions or accumulation of conductive ore
715 minerals resulting from hydrothermal circulation can significantly reduce electrical resistivity in
716 shear- and fault zones (Biswas et al., 2014; Unsworth & Bedrosian, 2004). All inversion

approaches result in this vertical conductor. In the density-constrained resistivity model of JI1, however, the feature is significantly less pronounced and interrupted at ~20 km depth (Fig. 10b, anomaly C1). The conductor has a very small lateral extent, as seen in the top view (Fig. 11). Therefore, it seems to be backed mostly by data of one station (station 3), although the apparent resistivity of that station shows no obvious resistivity decrease compared to neighboring stations (see Figure 6, top row).

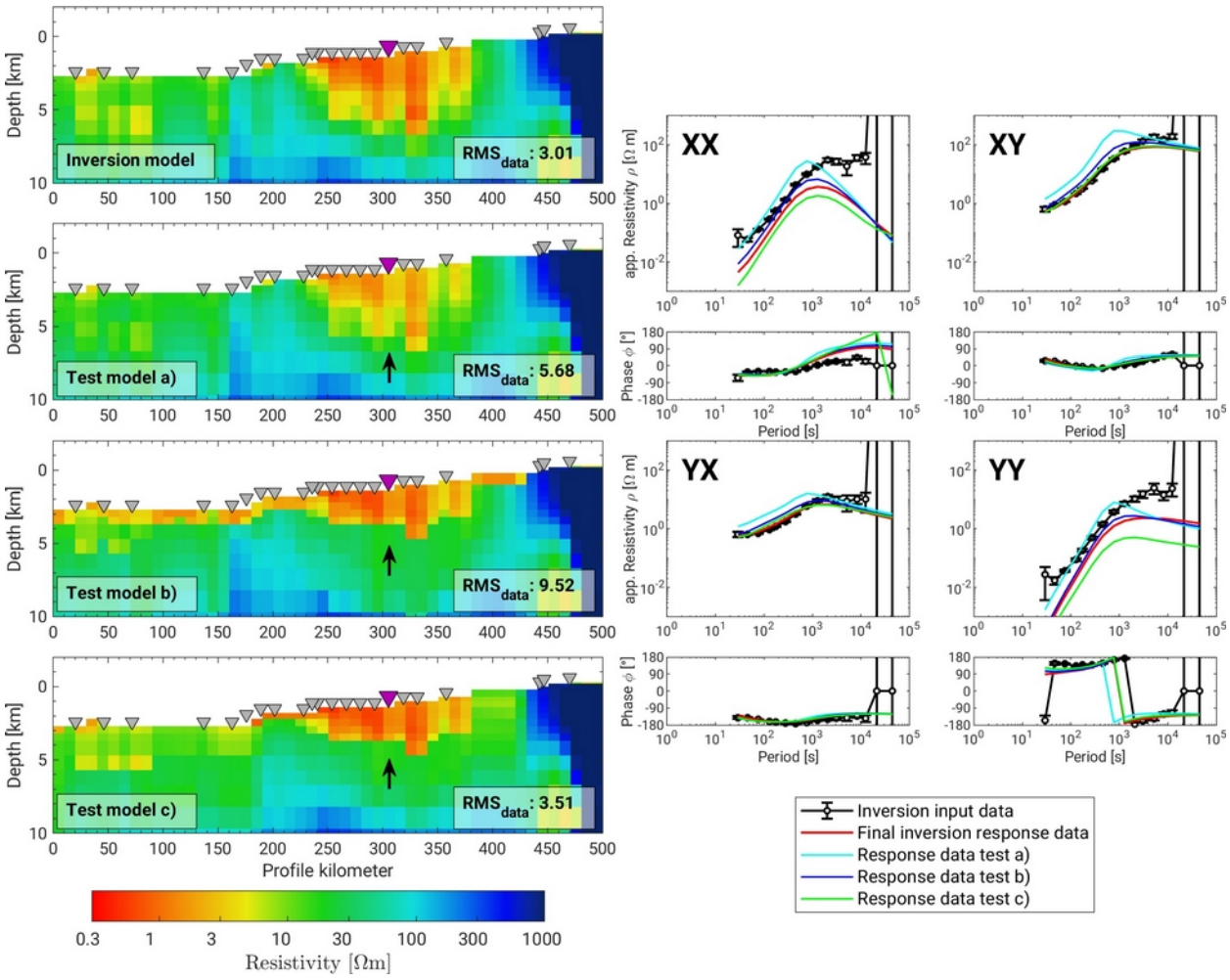

Figure 12. Depiction of test models and responses concerning sediment cover resistivity anomaly. The left panel shows slices through resistivity models along profile 100. Top: result of MT-only inversion. Second: Test a) increased resistivities in sediments. Third: Test b) thinner sediment cover. Bottom: Test c) thinner sediments with decreased resistivity. The right panel shows the response data of station 28 to the models depicted on the left. Station 28 is highlighted with a purple triangle on the model slices and black arrow indicate strong model changes.

729 In order to examine resolution capabilities for this feature, we performed similar tests as
730 with the sediment's resistivity responses. Models were modified by g) increasing the feature's
731 resistivity (every cell with a resistivity below 3.3 Ωm is increased by half its value) to test for the
732 general need of low resistivities; h) drastically decreasing the feature's depth (cells below 15 km
733 with resistivity below 10 Ωm are set to half-space resistivity of 50 Ωm) to challenge the extreme
734 depth of this conductor; and i) decreasing the feature's depth extent and significantly increasing
735 the resistivity at depth (below 15 km, all cells in the area are set to at least 1000 Ωm).
736 Additionally, in test i) the low resistivity anomaly is extended south and south-west, to form a
737 ridge-parallel elongated feature like a seaward-extending fracture zone. Figure 13 shows vertical
738 slices through the inversion- and test models along P3 alongside the response data for station 3
739 on this profile. Test g) has the strongest data misfit (the single RMS misfit for station 3 is 4.2,
740 compared to 3.0 in the original inversion model). This demonstrates the general need for a low
741 resistivity anomaly. Tests h) and i) have similar response curves (see Fig. 13, right) and only
742 deviate from each other and the original inversion response at short periods. As the calculations
743 of test h) show a better data fit than those of test i), we believe that the northern edge of Walvis
744 Ridge is in fact a frontier of a change in resistivity related to the change in crustal thickness
745 between the Angola basin and Walvis Ridge. This means, that deep resistivities north of Walvis
746 Ridge cannot be as high as those observed directly beneath the ridge at kilometers 150-230.
747 However, test model h) also indicates that the exceptionally low values at depths greater than 15
748 kilometers are not required to fit the MT data. The elongation of the conductor parallel to Walvis
749 Ridge (and the MT stations of P100) applied in test i), results in only small changes of the
750 response curves of nearby stations, which emphasizes once more the lack of resolution away
751 from MT stations.

752

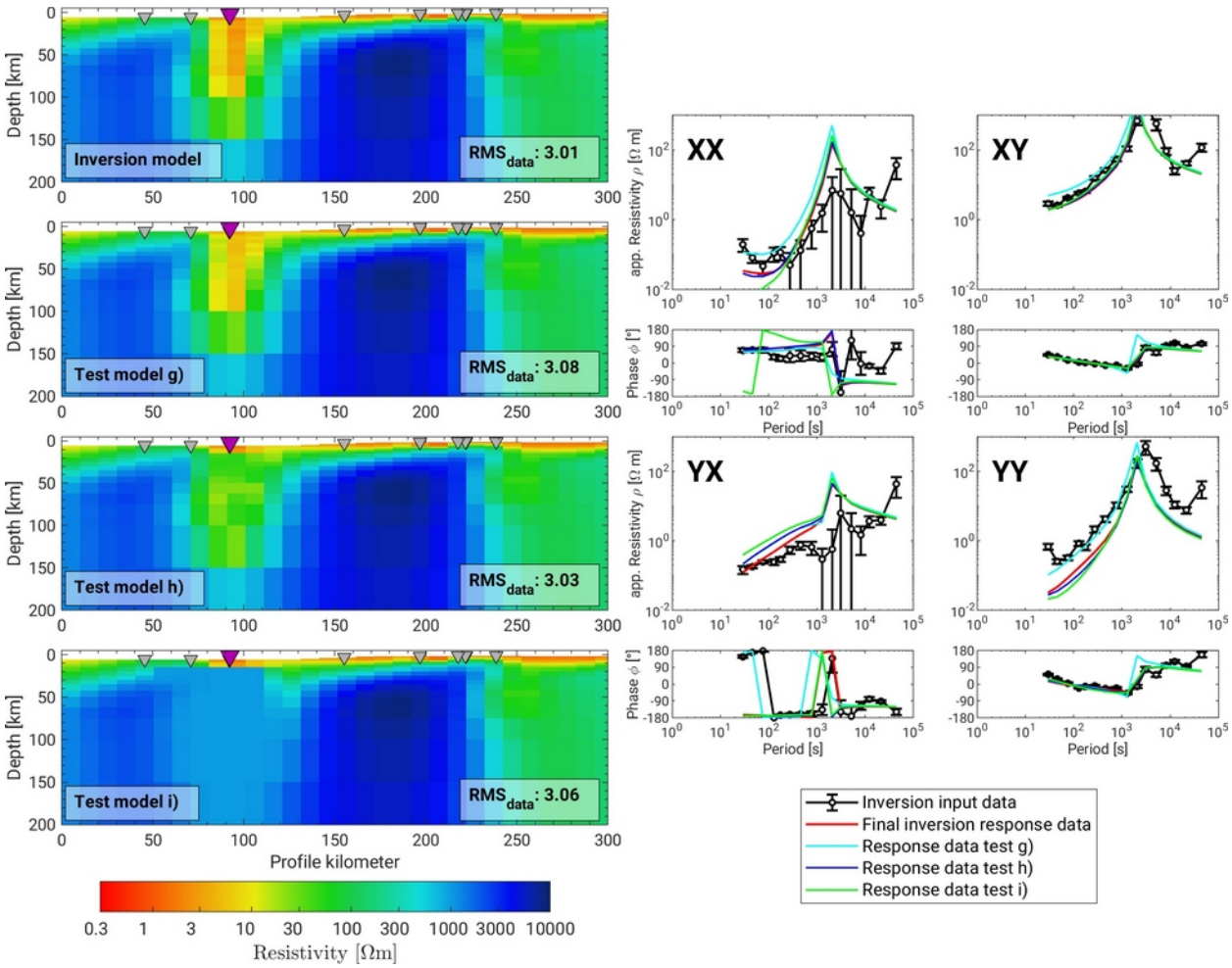

753 Figure 13. Depiction of test models and responses concerning fracture zone resistivity anomaly.
754 The left panel shows slices through resistivity models along profile 3. Top: result of MT-only
755 inversion. Second: Test g) increased resistivities of supposed fracture zone. Third: Test h)
756 conductor less deep. Bottom: Test i) shallow, elongated conductor with increased resistivities
757 beneath. The right panel shows the response data of station 3 to the models depicted on the left.
758 Station 3 is highlighted with a purple triangle on the model slices.

759 **5 Discussion**

760 Our analysis focuses on four different strategies of inverting the same MT data set with
761 and without additional constraints. The MT-only inversion is a re-evaluation of the results
762 presented in Jegen et al. (2016) for which a sign-error in the data rotation matrix was identified
763 after publication. The most important deviation of our new resistivity model compared to the
764 previously published model is the lack of a conductor ‘C’ (Fig. 5 in Jegen et al., 2016) between

765 the coast and profile 3, south of Walvis Ridge. Now, we observe these low resistivity zones only
766 close to the station's profiles (conductors C2 & C3 in Fig. 9 & 10). They are correlated to the
767 low apparent resistivities on stations 25-31 and 14-17 (Fig. 6). The sensitivity tests described
768 above show a limited resolution capability far away from MT stations. Thus, we conclude that
769 the rotation error has led to an exaggerated distortion of these shallow low resistivities. In order
770 to discuss the quality of the three integrated inversion approaches, we use the comparison of our
771 three resulting resistivity models with the constraining models used as well as their
772 interpretation. We compare the joint inversion models with independent seismic models and
773 other data in the region where possible. Other important criteria in the inversion comparison are
774 the MT data fit and model roughness as well as the data sensitivity tests described in the previous
775 section. All these criteria will be discussed for the different inversions JI1, JI2, and JI3 focusing
776 on the three main model features sediment cover (especially anomalies C2 & C3), magmatic
777 underplating (anomaly R) and Florianopolis Fracture Zone (anomaly C1). The constraining
778 models and independent data show the following features:

779 Seismic data along profile 100 (Fromm et al., 2017) show that there are up to 2 km-deep
780 sediment basins on top of Walvis Ridge that are separated by seamounts at profile kilometer
781 ~110 and ~180. This broadly agrees with Goslin et al. (1974)'s interpretation of at least 2.5 km-
782 thick sediment cover along two ridge-crossing profiles. Further east (220-340 km), Fromm et al.
783 (2017) identified reduced seismic velocities between 2 and 6 km depth, which correlate with the
784 connection of the northern most part of the Walvis Basin with the southern edge of Namibe
785 Basin (Stewart et al., 2000). Along the coast-parallel profile 3, Planert et al. (2016) imaged
786 slightly increased (~3 km) sediment thickness north of Walvis Ridge, and a sediment cover south
787 of the Ridge increasing in thickness from ~0.5 km at the northern edge of Walvis Ridge to
788 thicknesses larger than 2 km in Walvis Basin. Coast-perpendicular seismic profiles along the
789 Namibian margin south of Walvis Ridge (Bauer & Schulze, 1996; Elliott et al., 2009;
790 Gladczenko et al., 1998) show clear evidence for seaward dipping reflections (SDR) indicating
791 the presence of subaerial lava flows reaching thicknesses of ~7 km.

792 In the lower crust below Walvis Ridge, seismic studies reveal high seismic velocities
793 (Fromm et al., 2017; Planert et al., 2016) and Maystrenko et al. (2013) postulate a high-density
794 lower crustal body. The studies interpret these features as magmatic underplating. This may
795 coincide with an increase in electrical resistivity due to its low porosity and mafic nature, i.e.

depleted in incompatible elements and volatiles and rich in olivines and quartz (Eldholm et al., 2000; Gernigon et al., 2004; White & McKenzie, 1989). The seismic studies image thicknesses of this feature of ~8-15 km directly beneath the ridge and ~2-8 km south of it. In contrast, the structural density model by Maystrenko et al. (2013) predicts thicknesses of this layer to be in the range of ~10 to 30 km. Gladczenko et al. (1998) and Bauer et al. (2000) also image high-velocity underplating along the Namibian Margin south of Walvis Ridge of similar thickness. The upper boundary of underplating is located between 18 and 23 km depth in all models.

The last feature we compare with reference studies is the Florianopolis Fracture Zone north of Walvis Ridge. Its existence has been confirmed by various seismic studies (Fromm et al., 2017; Gladczenko et al., 1998; Goslin et al., 1974; Planert et al., 2016; Sibuet et al., 1984) as an abrupt decrease in crustal thickness and northward-increasing water depth. However, except for the lithospheric and crustal thickness variation across the fracture zone, there are no additional velocity or density anomalies.

The resistivity models of MT-only and joint MT-gravity data inversion (JI2) show almost no difference and identical MT data- and regularization misfits along with a low gravity data misfit. We attribute this observation to the fact that the gravity data can be fit very freely thus failing to reduce the MT solution space significantly. In fact, it is the MT inversion model which constrains the density model. Concerning the sediment cover along Walvis Ridge, we observe a deepening of sedimentary basins in the density model (e.g. profile 100 Fig. 9e, 220-570 km, and profile 3 Fig. 10e, 200-600 km) compared to the structural density model (Fig. 9 & 10c). The shallow low-resistivity anomalies C2 and C3 are imprinted onto the density model through the cross-gradient term. On profile 100 (Fig. 9d) the shallow conductive structures are laterally varying. Increased resistivities coincide with seamounts interrupting sediment cover, and conductors (e.g. C2) coincide with sediment basins observed in seismic and gravity studies (Fromm et al., 2017; Goslin et al., 1974; Stewart et al., 2000; cp. Fig. 9). The conductor's thickness of up to 10 km clearly exceeds the references' values of ~2-6 km. Low resistivity anomalies C3 along profile 3 between 240-300 and 320-370 km correspond to seaward dipping reflectors imaged on transects 2 and 3 in Gladczenko et al. (1998). The conductive anomalies reach ~10 km thickness, slightly exceeding the ~7 km stated by references. For the second model feature, the large mid-crustal resistor R, lateral extent of high resistivities/densities along the profile is well matched by observations of Fromm et al. (2017), Gladczenko et al. (1998),

827 Maystrenko et al. (2013), and Planert et al. (2016). In our JI2 resistivity model, the top of R is
828 located slightly higher (at ~15-20 km depth) than in the reference models. While underplating is
829 bounded by the Moho in the seismic models, no distinct bottom, and therefore thickness, can be
830 identified in the resistivity model. This observation is consistent with our sensitivity tests that
831 support high resistivity values at depths below Moho. The lack of an electrical resistivity contrast
832 across the seismic Moho is a common feature indicating that the electrical resistivity is governed
833 more by the pore space volume than chemical differences in the rocks (Jones, 2013; Wang et al.,
834 2013). The JI2 inversion of the gravity data results in a density anomaly model, i.e. the
835 difference of the resulting inversion and the earth reference model . Thus, interpretation of the
836 final absolute density models (as shown in Figures 9, 10 and 11) has to take into account, that the
837 sharp, constant model (reference + correction model, see Fig. 4) is added to a smoothed anomaly
838 model. This may result in artificial structural boundaries caused by the fixed block boundaries in
839 the reference- and correction model. For instance, the observed high densities (>3.3 g/cm^3)
840 directly beneath the Moho (dark blue colors in Figures 9 and 10e), could be either an indication
841 for increased upper mantle densities, or an indication of a slightly thinner crust. The seismic
842 velocity models by Fromm et al. (2017) and Planert et al. (2016) (black lines in the mentioned
843 figures) image indeed a shallower Moho, which points to the latter.

844 The observed resistivity decrease below 80 – 100 km is only poorly resolved, yet these
845 depths are in good agreement with the proposed lithosphere-asthenosphere boundary in this
846 region (Fishwick, 2010; Maystrenko et al., 2013). The location of the vertical conductor C1
847 along profile 3 in the joint data inversion (JI2) coincides with the identified change in crustal
848 thickness and composition, however the reference studies do not reveal velocity or density
849 anomalies. This strong vertical resistivity feature is also imprinted through cross-gradient
850 coupling onto the density model, although previous gravity studies have not observed a density
851 anomaly. The large residual along the Florianopolis Fracture Zone (Fig. 8c) indicates that this
852 density anomaly rather contradicts the gravity data than fitting it, which is why we believe it is
853 an artifact caused by the cross-gradient coupling. Many models can fit the gravity data. This
854 means, that gravity inversion with cross-gradient coupling is a weak constraint in joint inversion.
855 It may lead to a strong imprint of resistivity structures on the inverted density model. An
856 example is the slightly enhanced outline of conductor C1 in Figure 10d compared to 10a.

An alternative scheme of incorporating density data in MT inversion is coupling a fixed structural density model to the MT data inversion (JI1). The resistivity model resulting from this approach shows some significant model differences compared to the MT-only inversion model, while reaching an almost identical MT data fit. The increased roughness in the resulting resistivity model is clearly visible in the vertical slices in Figures 9 and 10b, and may be explained by the sharp boundaries in the blocky density cross-model (Fig. 9 and 10c). Higher roughness is also evident in the increased regularization term of the objective function compared to MT-only or joint data inversion JI2 (see Fig. 5). For the sedimentary layer, the interfaces introduced in the shallow conductors along profile 100 at ~3-5 km depth (Fig. 9b) are in accordance with the sediment thickness derived from seismic imaging by Fromm et al. (2017) and Goslin et al. (1974). Seismic imaging has a very good resolution of structural boundaries and it is unlikely that the seismic velocity used for depth conversion of the reflector is very far off. Thus, the shallower seismically derived depth to basement seems more realistic than the depth derived from the MT models. As the sensitivity tests described above showed, the MT data cannot resolve the thickness and conductivity of the shallow sediments independently, but only its conductance, i.e. the thickness conductivity product. Thus, the resistivity model can be matched to seismic models by decreasing the sediment layer thickness while increasing its conductivity. However, the values required to match the sediment layer thickness imaged by seismic data would require some areas to have resistivities as low as 1 to 2 Ωm down to a depth of 5 km. Such average low resistivities are difficult to conceive for old thick sedimentary basins. In this structurally constrained inversion JI1, an additional conductor is placed within the basement underneath the sediments to account for the higher conductance required by the MT data. This could indicate the presence of thin, conductive layers in the upper crust, not resolved by gravity and seismic methods. Alternatively, initial smoothing followed by cross-gradient driven introduction of boundaries and the MT method's sensitivity of conductance could lead to artifacts below the actual sediment base. Along profile 3, the areas of increased thickness in the conductive layer correlate with seismic observations of seaward dipping reflections (conductors C3, Fig. 10b). They include less pronounced shallow boundaries, which indicates that those conductors and their thickness is more reliable. We propose that the conductive incisions C3 in the continuous sediment layer south of Walvis Ridge are caused by inter-layered magmatic flows and sediments. The high resistivity values directly beneath those anomalies might indicate

former pathways for magmatic material, which erupted episodically to form the alternating magmatic-sedimentary sequences (Elliott et al., 2009; Planke et al., 2000). The highest resistivity values associated with magmatic underplating are further seaward (Fig. 9b, resistor R). However, as a clear distinction of resistivities above ~2000 Ωm is difficult this apparent shift may be artificial. The structural cross model also imprints the horizontal Moho boundary onto the resistivity model (anomaly R, Fig. 9 & 10b). However, the variation in resistivity is rather small, but according to our sensitivity test g) a strong resistivity contrast at the seismic Moho is not compatible with the MT data. Thus, the smaller off-axis horizontal extent of this resistor, i.e. high values are confined to areas close to MT stations, cp. Fig. 11b, contradicts seismic observations of high velocity magmatic underplating all along the Namibian margin (Bauer et al., 2000; Gladczenko et al., 1998). The sensitivity tests h) and i) indicate limited resolution off-profile axis. Therefore, we conclude that cross-gradient coupling of the fixed structural cross-model used in this approach, causes this restriction due to the model's large blocks with constant density. Within these blocks no gradients are enforced by cross-gradient coupling, and the resistivity inversion model remains mostly at starting model conditions where MT sensitivity is reduced. The observed weakening of anomaly C1, associated with the Florianopolis Fracture Zone challenges the existence of the great vertical extent of this feature in the MT-only and JI2 models. The presence of the strong low-resistivity anomaly in this region and the absence of a matching velocity or density anomaly is enigmatic. One possible explanation may be a bias in the data of the MT stations sensitive to the anomaly or insufficient bathymetric resolution to account for the strong topography in the area. Key & Constable (2011) and Worzewski et al. (2012) describe the distortion of MT response by an adjacent coast. We propose that a similar effect, i.e. the sudden change in water depth, may be responsible for the magnitude of the conductive anomaly. This "coast effect" is manifested in the measured data in form of a strong apparent resistivity cusp and phase jumps. Forward model responses of our simple starting model (including bathymetry and sediment cover) cannot account for these strong effects, which forces the inversion to include strong anomalies in the model. In the top view (Fig. 11), similar small scale, deep conductors are also visible close to stations 10 (just south of the profile crossing), and 23 (southern most), where lithological structure or water depth also change abruptly. Both of these features are significantly less pronounced in the density model constrained resistivity model (Fig. 11b), supporting the assumption of a "coast effect" artifact, which is effectively

suppressed by the coupling with a fixed structural cross-model. An alternative explanation for conductor C1 could be that a geological feature in this region is only associated with a resistivity anomaly, but not with a seismic or gravity anomaly. Such a process could be a difference in thermal subsidence between Walvis Ridge and the adjoining oceanic crust in the North creating fractures and allowing seawater to enter deep into the crust at the fracture zone. The already described sensitivity tests demonstrate that shallow low resistivities are needed for a reasonable MT data fit, but that those low values do not necessarily have to reach deep into the mantle but may be confined to the top 15-20 kilometers only. Crustal alteration down to this depth would be conceivable.

The last inversion approach JI3, in which the fixed velocity model by Fromm et al. (2017) was used as the cross-model for a cross-gradient constrained inversion, differs from the previous coupling strategies because we performed a “quasi-2D” inversion on a narrow cube along profile P100 that strikes perpendicular to the coast. We conducted this coupling on the one hand to test the influence of different types of cross-models (i.e. blocky density versus smooth gradient velocity), and on the other hand to explore whether we can find an MT model which fits those seismic observations. However, the different model scope and input data for the inversions make a direct comparison of the RMS data misfit impossible. To evaluate the misfit anyhow, we cut the central part around profile 100 from the other three 3D inversion models and calculated the misfit for these “quasi-2D” models and the data of these 23 stations only. The data misfits for these MT-only, density constrained (JI1), and joint data inversion (JI2) resistivity models are all approximately 4.4, while the MT-only inversion for narrow model reaches a minimum misfit of 3.84. We therefore conclude that the RMS of 4.03 that was reached with JI3, is acceptable. The discrepancy of ~0.2 to the MT-only inversion indicates that this form of coupling is the strongest constraint used in our study, because we could not reach the same low misfit attained by unconstrained inversion. The velocity model may not change during inversion and since it has fewer areas of constant value (compared to the density cross model in JI1), the MT solution space is confined most. Model roughness is significantly reduced compared to the density model-coupled inversion. This increased smoothness originates from the nature of the gradient velocity model, which has fewer strong boundaries. However, the cross-model’s strong gradients at the sediment-crust interface still introduce some patchiness in the upper part of the resistivity model. Just as observed in the resistivity model of JI1, the introduced boundaries in the shallow

conductors indicate thinner sediment cover compared to the MT-only resistivity model (anomaly C2 in Fig. 9f). They are in good agreement with seismic observations and robust according to our sensitivity analysis. At the seismically imaged Moho depth, the resistivity model shows no variation, which may be explained by the smaller velocity gradient between crust and mantle, compared to the strong gradients in the upper part of the section which corresponds to a weaker cross-gradient coupling. Based on our sensitivity test d) (reducing the resistor's thickness), we conclude that the resistivity structure does not change a lot at Moho depth, while seismic reflections clearly show a change in acoustic impedance. The weak cross-gradient coupling at this interface therefore serves our inversion results, because it does not enforce a false resistivity contrast.

6 Conclusion

The cross-gradient coupled inversion with a structural density model constraint (JI1) works best for the Namibia and Walvis Ridge MT data inversion. This inversion draws on the benefits from gravity modeling and includes a significant amount of information from seismic results, both directly and indirectly because Maystrenko et al. (2013) used seismic models to build their initial density model. This joint inversion results in geologically valuable model modifications such as thinner conductive sediment cover or intra-basement conductors, and a less pronounced impact of the Florianopolis Fracture Zone on electrical resistivity. Importantly, the resulting model has not only more details than a MT-only inversion, but also a higher confidence because it is constrained by several data sets while reaching almost the same misfit between the forward modeled data and the observed data.

Combining gravity inversion with the weak cross-gradient coupling in joint inversion (JI2) results in only small modifications of the final resistivity model that will not change the geological interpretation. The large solution space of gravity data inversion cannot sufficiently constrain MT inversion. The density model shows mainly modifications mainly on model features, which we mistrust (i.e. up to 10 km deep sedimentary basins and density variations along a fracture zone reaching 150 km deep into the mantle). Direct parameter coupling may improve the joint MT-gravity data inversion in the future, but defining precise resistivity-density relationships in this large, complex area appears extremely difficult.

The use of a gradual velocity model rather than a blocky density model for cross-gradient constrained inversions (JI3) is promising, because the inversion resistivity model is also based on smooth gradients, thus model roughness is decreased in the resulting resistivity model. This fixed-model joint inversion poses the strongest constraint in our study. However, the assumption of a "quasi-2D" inversion is not ideal and the low misfits of a full 3D inversion cannot be reached.

Acknowledgments

The Acquisition of the MT data used in this work was supported by the German Research Foundation (DFG) as part of the Priority Program SPP1375 and the Future Ocean Program of Kiel Marine Sciences. We thank the captain and the crew of R/V Maria S. Merian for the professional and friendly support of the scientific work in the cruises. We thank our partnering institute GFZ Potsdam (especially Ute Weckmann, Oliver Ritter, and Magdalena Scheck-Wenderoth) and Tanja Fromm for their collaboration and the possibility to use their data or models. Further thanks go to Anne Neska, Gerhard Kapinos, and Anna Martí for processing of the marine MT data. The computations were performed using the NESH High Performance Computing Facility at Kiel University.

The marine magnetotelluric dataset for this research will be available in the PANGAEA data repository upon acceptance. Satellite gravity data is available from ICGEM.

References

Amante, C., & Eakins, B. W. (2009). ETOPO1 1 Arc-Minute Global Relief Model: Procedures, Data Sources and Analysis. NOAA Technical Memorandum NESDIS NGDC-24. National Geophysical Data Center, NOAA. https://doi.org/10.7289/V5C8276M

Andersen, O. B., Knudsen, P., & Berry, P. A. M. (2010). The DNSC08GRA global marine gravity field from double retracked satellite altimetry. *Journal of Geodesy*, *84*(3), 191–199. https://doi.org/10.1007/s00190-009-0355-9

1006 Avdeev, D., & Avdeeva, A. (2009). 3D magnetotelluric inversion using a limited-memory quasi-
1007 Newton optimization. *Geophysics*, *74*(3), F45–F57. https://doi.org/10.1190/1.3114023

1008 Avdeev, D. B., Kuvshinov, A. V., Pankratov, O. V., & Newman, G. A. (1997). High-
1009 Performance Three-Dimensional Electromagnetic Modelling Using Modified Neumann
1010 Series. Wide-Band Numerical Solution and Examples. *Journal of Geomagnetism and*
1011 *Geoelectricity*, *49*(11), 1519–1539. https://doi.org/10.5636/jgg.49.1519

1012 Avdeeva, A., & Avdeev, D. (2006). A limited-memory quasi-Newton inversion for 1D
1013 magnetotellurics. *Geophysics*, *71*(5). https://doi.org/10.1190/1.2236381

1014 Barthelmes, F., & Köhler, W. (2016). International Centre for Global Earth Models (ICGEM). In
1015 *The Geodesists Handbook 2016* (pp. 907–1205). https://doi.org/10.1007/s00190-016-0948-z

1016 Bauer, K, & Schulze, A. (1996). Seismic investigations of the passive continental margin of
1017 Namibia from wide-angle on-shore off-shore data. *EOS Trans AGU*, *77*, F669.

1018 Bauer, Klaus, Neben, S., Schreckenberger, B., Emmermann, R., Hinz, K., Fechner, N., et al.
1019 (2000). Deep structure of the Namibia continental margin as derived from integrated
1020 geophysical studies. *Journal of Geophysical Research: Solid Earth*, *105*(B11), 25829–
1021 25853. https://doi.org/10.1029/2000jb900227

1022 Becken, M., & Burkhardt, H. (2004). An ellipticity criterion in magnetotelluric tensor analysis.
1023 *Geophysical Journal International*, *159*(1), 69–82. https://doi.org/10.1111/j.1365-
1024 246X.2004.02376.x

1025 Bedrosian, P. A. (2007). MT+, integrating magnetotellurics to determine earth structure, physical
1026 state, and processes. *Surveys in Geophysics*, *28*(2–3), 121–167.
1027 https://doi.org/10.1007/s10712-007-9019-6

1028 Biswas, A., Mandal, A., Sharma, S. P., & Mohanty, W. K. (2014). Delineation of subsurface
1029 structures using self-potential, gravity, and resistivity surveys from South Purulia Shear
1030 Zone, India: Implication to uranium mineralization. *Interpretation*, *2*(2), T103–T110.
1031 https://doi.org/10.1190/INT-2013-0170.1

1032 Candansayar, M. E., & Tezkan, B. (2008). Two-dimensional joint inversion of
1033 radiomagnetotelluric and direct current resistivity data. *Geophysical Prospecting*, *56*(5),
1034 737–749. https://doi.org/10.1111/j.1365-2478.2008.00695.x

1035 Chave, A. D., & Thomson, D. J. (2004). Bounded influence magnetotelluric response function
1036 estimation. *Geophysical Journal International*, *157*(3), 988–1006.
1037 https://doi.org/10.1111/j.1365-246X.2004.02203.x

1038 Cohen, C., & Smith, D. E. (1985). LAGEOS Scientific Results: Introduction. *Journal of*
1039 *Geophysical Research*, *90*, 9217–9220.

1040 Colombo, D., & Rovetta, D. (2018). Coupling strategies in multiparameter geophysical joint
1041 inversion. *Geophysical Journal International*. https://doi.org/10.1093/GJI/GGY341

1042 Drinkwater, M. R., Haagmans, R., Muzi, D., Popescu, A., Floberghagen, R., Kern, M., &
1043 Fehringer, M. (2007). The GOCE gravity mission: ESA'S first core earth explorer.
1044 *European Space Agency, (Special Publication) ESA SP*, (SP-627), 1–7.

1045 Egbert, G. D. (1997). Robust multiple-station magnetotelluric data processing. *Geophysical*
1046 *Journal International*, *130*(2), 475–496. https://doi.org/10.1111/j.1365-
1047 246X.1997.tb05663.x

1048 Eldholm, O., Gladczenko, T. P., Skogseid, J., & Planke, S. (2000). Atlantic volcanic margins: A
1049 comparative study. *Geological Society Special Publication*, *167*, 411–428.
1050 https://doi.org/10.1144/GSL.SP.2000.167.01.16

1051 Elliott, G. M., Berndt, C., & Parson, L. M. (2009). The SW African volcanic rifted margin and
1052 the initiation of the Walvis Ridge, South Atlantic. *Marine Geophysical Research*, *30*(3),
1053 207–214. https://doi.org/10.1007/s11001-009-9077-x

1054 Ferguson, I. J., Lilley, F. E. M., & Filloux, J. H. (1990). Geomagnetic induction in the Tasman
1055 Sea and electrical conductivity structure beneath the Tasman Seafloor. *Geophysical Journal*
1056 *International*, *102(2*), 299–312. https://doi.org/10.1111/j.1365-246X.1990.tb04468.x

1057 Fishwick, S. (2010). Surface wave tomography: Imaging of the lithosphere - asthenosphere
1058 boundary beneath central and southern Africa? *Lithos*, *120*(1), 63–73.

1059 Förste, C., Bruinsma, S., Abrikosov, O., Flechtner, F., Marty, J.-C., Lemoine, J.-M., et al. (2014).
1060 EIGEN-6C4 - The latest combined global gravity field model including GOCE data up to
1061 degree and order 2190 of GFZ Potsdam and GRGS Toulouse. *EGU General Assembly*.
1062 https://doi.org/http://dx.doi.org/10.5880/icgem.2015.1

1063 Fromm, T, Jokat, W., Ryberg, T., Behrmann, J. H., Haberland, C., & Weber, M. (2017). The
1064 onset of Walvis Ridge: Plume influence at the continental margin. *Tectonophysics*.

1065 Fromm, Tanja, Planert, L., Jokat, W., Ryberg, T., Behrmann, J. H., Weber, M. H., & Haberland,
1066 C. (2015). South Atlantic opening: A plume-induced breakup? *Geology*, *43*(10), 931–934.
1067 https://doi.org/10.1130/G36936.1

1068 Gallardo, L. A., & Meju, M. A. (2003). Characterization of heterogeneous near-surface materials
1069 by joint 2D inversion of dc resistivity and seismic data. *Geophysical Research Letters*,
1070 *30*(13). https://doi.org/10.1029/2003GL017370

1071 Gernigon, L., Ringenbach, J. C., Planke, S., & Le Gall, B. (2004). Deep structures and breakup
1072 along volcanic rifted margins: Insights from integrated studies along the outer Vøring Basin
1073 (Norway). *Marine and Petroleum Geology*, *21*(3), 363–372.
1074 https://doi.org/10.1016/j.marpetgeo.2004.01.005

1075 Gladczenko, T. P., Skogseid, J., & Eldhom, O. (1998). Namibia volcanic margin. *Marine*
1076 *Geophysical Research*, *20*(4), 313–341. https://doi.org/10.1023/A:1004746101320

1077 Goslin, J., Mascle, J., Sibuet, J.-C., & Hoskins, H. (1974). Geophysical study of the easternmost
1078 Walvis Ridge, South Atlantic: Morphology and shallow structure. *Geological Society of*
1079 *America Bulletin*, *85*(4), 619–632. https://doi.org/10.1130/0016-
1080 7606(1974)85<619:GSOTEW>2.0.CO;2

1081 Gotze, H. J., & Lahmeyer, B. (1988). Application of three-dimensional interactive modeling in
1082 gravity and magnetics. *Geophysics*, *53*(8), 1096–1108. https://doi.org/10.1190/1.1442546

1083 Günther, T., & Rücker, C. (2006). A new joint inversion approach applied to the combined
1084 tomography of DC resistivity and seismic refraction data. *19th Symposium on the*
1085 *Application of Geophysics to Engineering and Environmental Problems, SAGEEP 2006:*

1086 *Geophysical Applications for Environmental and Engineering Hazzards - Advances and*
1087 *Constraints*, *2*, 1196–1202. https://doi.org/10.4133/1.2923578

1088 Heincke, B., Jegen, M., Moorkamp, M., Hobbs, R. W., & Chen, J. (2017). An adaptive coupling
1089 strategy for joint inversions that use petrophysical information as constraints. *Journal of*
1090 *Applied Geophysics*, *136*, 279–297. https://doi.org/10.1016/j.jappgeo.2016.10.028

1091 Heit, B., Yuan, X., Weber, M., Geissler, W., Jokat, W., Lushetile, B., & Hoffmann, K. H. (2015).
1092 Crustal thickness and Vp/Vs ratio in NW Namibia from receiver functions: Evidence for
1093 magmatic underplating due to mantle plume-crust interaction. *Geophysical Research*
1094 *Letters*, *42*(9), 3330–3337. https://doi.org/10.1002/2015GL063704

1095 Ince, E. S., Barthelmes, F., Reißland, S., Elger, K., Förste, C., Flechtner, F., & Schuh, H. (2019).
1096 ICGEM – 15 years of successful collection and distribution of global gravitational models,
1097 associated services, and future plans. *Earth System Science Data*, *11*(2), 647–674.
1098 https://doi.org/10.5194/essd-11-647-2019

1099 Jegen, M., Avdeeva, A., Berndt, C., Franz, G., Heincke, B., Hölz, S., et al. (2016). 3-D
1100 magnetotelluric image of offshore magmatism at the Walvis Ridge and rift basin.
1101 *Tectonophysics*, *683*, 98–108. https://doi.org/10.1016/j.tecto.2016.06.016

1102 Jones, A. G. (2013). Imaging and observing the electrical Moho. *Tectonophysics*, *609*, 423–436.
1103 https://doi.org/10.1016/j.tecto.2013.02.025

1104 Kalscheuer, T., Blake, S., Podgorski, J. E., Wagner, F., Green, A. G., Maurer, H., et al. (2015).
1105 Joint inversions of three types of electromagnetic data explicitly constrained by seismic
1106 observations: Results from the Central Okavango Delta, Botswana. *Geophysical Journal*
1107 *International*, *202*(3), 1429–1452. https://doi.org/10.1093/gji/ggv184

1108 Kapinos, G., Weckmann, U., Jegen-Kulcsar, M., Meqbel, N., Neska, A., Katjiuongua, T. T., et
1109 al. (2016). Electrical resistivity image of the South Atlantic continental margin derived from
1110 onshore and offshore magnetotelluric data. *Geophysical Research Letters*, *43*(1), 154–160.
1111 https://doi.org/10.1002/2015GL066811

1112 Key, K., & Constable, S. (2011). Coast effect distortion of marine magnetotelluric data: Insights
1113 from a pilot study offshore northeastern Japan. *Physics of the Earth and Planetary Interiors*,
1114 *184*(3–4), 194–207. https://doi.org/10.1016/j.pepi.2010.11.008

1115 Laske, G., Masters, G., Ma, Z., & Pasyanos, M. (2013). Update on CRUST1.0---A 1-degree
1116 global model of Earth's crust. In *EGU General Assembly 2013* (Vol. 15, p. 2658). Vienna.
1117 Retrieved from http://meetingorganizer.copernicus.org/EGU2013/EGU2013-2658.pdf

1118 Mandolesi, E., & Jones, A. G. (2014). Magnetotelluric inversion based on mutual information.
1119 *Geophysical Journal International*, *199*(1), 242–252. https://doi.org/10.1093/gji/ggu258

1120 Martí, A., Queralt, P., & Ledo, J. (2009). WALDIM: A code for the dimensionality analysis of
1121 magnetotelluric data using the rotational invariants of the magnetotelluric tensor.
1122 *Computers & Geosciences*, *35*(12), 2295–2303. https://doi.org/10.1016/j.cageo.2009.03.004

1123 Maystrenko, Y. P., Scheck-Wenderoth, M., Hartwig, A., Anka, Z., Watts, A. B., Hirsch, K. K., &
1124 Fishwick, S. (2013). Structural features of the Southwest African continental margin
1125 according to results of lithosphere-scale 3D gravity and thermal modelling. *Tectonophysics*,
1126 *604*, 104–121. https://doi.org/10.1016/j.tecto.2013.04.014

1127 Moorkamp, M., Avdeeva, A., Basokur, A. T., & Erdogan, E. (2020). Inverting magnetotelluric
1128 data with distortion correction-stability, uniqueness and trade-off with model structure.
1129 *Geophysical Journal International*, *222*(3), 1620–1638. https://doi.org/10.1093/gji/ggaa278

1130 Moorkamp, Max. (2017). Integrating Electromagnetic Data with Other Geophysical
1131 Observations for Enhanced Imaging of the Earth: A Tutorial and Review. *Surveys in*
1132 *Geophysics*, *38*(5), 935–962. https://doi.org/10.1007/s10712-017-9413-7

1133 Moorkamp, Max, Jegen, M., Roberts, A., & Hobbs, R. (2010). Massively parallel forward
1134 modeling of scalar and tensor gravimetry data. *Computers & Geosciences*, *36*(5), 680–686.
1135 https://doi.org/10.1016/j.cageo.2009.09.018

1136 Moorkamp, Max, Heincke, B., Jegen, M., Roberts, A. W., & Hobbs, R. W. (2011). A framework
1137 for 3-D joint inversion of MT, gravity and seismic refraction data. *Geophysical Journal*
1138 *International*, *184*(1), 477–493. https://doi.org/10.1111/j.1365-246X.2010.04856.x

1139 Mosegaard, K., & Tarantola, A. (1995). Monte Carlo sampling of solutions to inverse problems.
1140 *Journal of Geophysical Research*, *100*(B7). https://doi.org/10.1029/94jb03097

1141 Nocedal, J., & Wright, S. (2006). *Numerical Optimization*. Springer-Verlag New York.
1142 https://doi.org/10.1007/978-0-387-40065-5

1143 Parolai, S., Picozzi, M., Richwalski, S. M., & Milkereit, C. (2005). Joint inversion of phase
1144 velocity dispersion and H/V ratio curves from seismic noise recordings using a genetic
1145 algorithm, considering higher modes. *Geophysical Research Letters*, *32*(1), 1–4.
1146 https://doi.org/10.1029/2004GL021115

1147 Planert, L., Behrmann, J., Jokat, W., Fromm, T., Ryberg, T., Weber, M., & Haberland, C. (2016).
1148 The wide-angle seismic image of a complex rifted margin, offshore North Namibia:
1149 Implications for the tectonics of continental breakup. *Tectonophysics*.

1150 Planke, S., Symonds, P. A., Alvestad, E., & Skogseid, J. (2000). Seismic volcanostratigraphy of
1151 large-volume basaltic extrusive complexes on rifted margins. *Journal of Geophysical*
1152 *Research: Solid Earth*, *105*(B8), 19335–19351. https://doi.org/10.1029/1999jb900005

1153 Podvin, P., & Lecomte, I. (1991). Finite difference computation of traveltimes in very contrasted
1154 velocity models: a massively parallel approach and its associated tools. *Geophysical*
1155 *Journal International*, *105*(1), 271–284. https://doi.org/10.1111/j.1365-
1156 246X.1991.tb03461.x

1157 Ritter, O., Junge, A., & Dawes, G. J. K. (1998). New equipment and processing for
1158 magnetotelluric remote reference observations. *Geophysical Journal International*, *132*(3),
1159 535–548. https://doi.org/10.1046/j.1365-246X.1998.00440.x

1160 Shi, Z., Hobbs, R. W., Moorkamp, M., Tian, G., & Jiang, L. (2017). 3-D cross-gradient joint
1161 inversion of seismic refraction and DC resistivity data. *Journal of Applied Geophysics*, *141*,
1162 54–67.

1163 Sibuet, J. C., Hay, W. W., Prunier, A., Montadert, L., Hinz, K., & Fritsch, J. (1984). Early
1164 evolution of the South Atlantic Ocean: role of the rifting episode. *Initial Reports DSDP, Leg*
1165 *75, Walvis Bay to Recife. Part 1*, 469–481. https://doi.org/10.2973/dsdp.proc.75.107.1984

1166 Stewart, J., Watts, A. B., & Bagguley, J. G. (2000). Three-dimensional subsidence analysis and
1167 gravity modelling of the continental margin offshore Namibia. *Geophysical Journal*
1168 *International*, *141*(3), 724–746. https://doi.org/10.1046/j.1365-246X.2000.00124.x

1169 Tapley, B. D., Bettadpur, S., Watkins, M., & Reigber, C. (2004). The gravity recovery and
1170 climate experiment: Mission overview and early results. *Geophysical Research Letters*,
1171 *31*(9), 1–4. https://doi.org/10.1029/2004GL019920

1172 Tarantola, A. (2005). *Inverse Problem Theory and Methods for Model Parameter Estimation*.
1173 *Inverse Problem Theory and Methods for Model Parameter Estimation*. Society for
1174 Industrial and Applied Mathematics. https://doi.org/10.1137/1.9780898717921

1175 Uieda, L., Barbosa, V. C. F., & Braitenberg, C. (2016). Tesseroids: Forward-modeling
1176 gravitational fields in spherical coordinates. *GEOPHYSICS*, *81*(5), F41–F48. https://doi.org/
1177 10.1190/geo2015-0204.1

1178 Ulrych, T. J., Sacchi, M. D., & Woodbury, A. (2001). A Bayes tour of inversion: A tutorial.
1179 *Geophysics*, *66*(1), 55–69. https://doi.org/10.1190/1.1444923

1180 Um, E. S., Commer, M., & Newman, G. A. (2014). A strategy for coupled 3D imaging of large-
1181 scale seismic and electromagnetic data sets: Application to subsalt imaging. *Geophysics*,
1182 *79*(3), 1–13. https://doi.org/10.1190/GEO2013-0053.1

1183 Unsworth, M., & Bedrosian, P. A. (2004). On the geoelectric structure of major strike-slip faults
1184 and shear zones. *Earth, Planets and Space*, *56*(12), 1177–1184.
1185 https://doi.org/10.1186/BF03353337

1186 Wang, Q., Bagdassarov, N., & Ji, S. (2013). The Moho as a transition zone: A revisit from
1187 seismic and electrical properties of minerals and rocks. *Tectonophysics*, *609*, 395–422.
1188 https://doi.org/10.1016/j.tecto.2013.08.041

1189 Weckmann, U., Magunia, A., & Ritter, O. (2005). Effective noise separation for magnetotelluric
1190 single site data processing using a frequency domain selection scheme. *Geophysical Journal*
1191 *International*, *161*(3), 635–652. https://doi.org/10.1111/j.1365-246X.2005.02621.x

White, R., & McKenzie, D. (1989). Magmatism at rift zones: The generation of volcanic continental margins and flood basalts. *Journal of Geophysical Research*, *94*(B6), 7685. https://doi.org/10.1029/JB094iB06p07685

Worzewski, T., Jegen, M., & Swidinsky, A. (2012). Approximations for the 2-D coast effect on marine magnetotelluric data. *Geophysical Journal International*, *189*(1), 357–368. https://doi.org/10.1111/j.1365-246X.2012.05385.x

Zelt, C. A. (1999). Modelling strategies and model assessment for wide-angle seismic traveltime data. *Geophysical Journal International*, *139*(1), 183–204. https://doi.org/10.1046/j.1365-246X.1999.00934.x

Zhou, J., Meng, X., Guo, L., & Zhang, S. (2015). Three-dimensional cross-gradient joint inversion of gravity and normalized magnetic source strength data in the presence of remanent magnetization. *Journal of Applied Geophysics*, *119*, 51–60. https://doi.org/10.1016/j.jappgeo.2015.05.001